

AD A030863

TN 3233

171-39331

1

TN  
3233

NAVAL ELECTRONICS LABORATORY CENTER SAN DIEGO CALIFORNIA 92152

EXPERIMENTAL TEST PLAN TO INVESTIGATE  
THE PROPAGATION OF BLUE/GREEN  
RADIATION THROUGH CLOUDS,

Technical Note

October 1, 1976

G. C. Mooradian, M. Geller,  
and L. B. Stotts, ~~5010~~ ~~Stotts~~  
Division (Code 2500),  
and H. G. Hughes, Propagation  
Division (Code 2200)

1 Oct 76

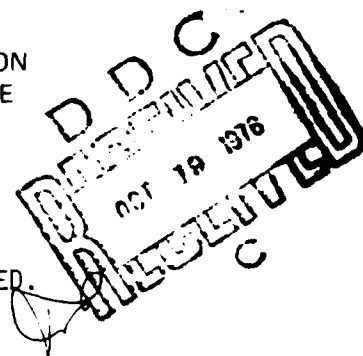
156

NELC-Z117

## NELC TECHNICAL NOTE

THIS IS A WORKING PAPER GIVING TENTATIVE INFORMATION  
ABOUT SOME WORK IN PROGRESS AT NELC. IF CITED IN THE  
LITERATURE THE INFORMATION IS TO BE IDENTIFIED AS  
TENTATIVE AND UNPUBLISHED.

APPROVED FOR PUBLIC RELEASE; DISTRIBUTION IS UNLIMITED.



DISTRIBUTION AVAILABLE TO OFFICES	
AND TO THE PUBLIC	
A	

102710

1R

## Contents

- 1.0 Introduction
- 2.0 Theoretical Background and Predictions
  - 2.1 Introduction
  - 2.2 Mie Scattering and the Radiative Transfer Equations
  - 2.3 Mutual Coherence Function
  - 2.4 Monte Carlo Computer Simulation
  - 2.5 Theoretical Results
- 3.0 Experimental Test Plan
  - 3.1 Goals of the Program
  - 3.2 Rationale for Selection of Site
  - 3.3 Proposed Measurements
  - 3.4 Description of Atmospheric Sensors
  - 3.5 Proposed Schedule
- 4.0 References

## 1.0 INTRODUCTION

CNO Operational Requirement XCC20 of 23 June 1975 establishes the need for low probability of intercept communications for installation aboard submarines and aircraft. In addition to covertness, a communication system is required to be independent of the submerged vehicle's speed and depth. Generally, submarines are antenna-limited in their communications. While several radio frequency systems are presently operational or undergoing OPEVAL/TECHEVAL, their use severely handicaps the submarine's speed and depth in direct support of surface units. While it is recognized that no single system can meet all Fleet requirements, only a submarine-to-aircraft optical communication system can achieve absolute covertness and speed independence. However, such a system is generally assumed to be only effectual in cloud-free environments; a limitation which greatly impairs the overall system capability. Yet the fact that sunlight gets through optically dense clouds on overcast days suggests that a sufficient amount of pulsed laser radiation might be available for demodulation/decoding after traversing the cloud if one made the field-of-view (FOV) of the receiver wide enough to collect the scattered irradiance. The effects of multiple scattering by dense atmospheric/marine clouds on pulsed radiation translates into a pulse stretching and spatial broadening of the initial signal. Thus the performance of any gated and continuous image viewing systems and communications systems using pulse-coding techniques will be degraded in terms of limited message data rates and reduced signal-to-noise ratios.

The Navy presently does not have sufficient information about the optical propagation properties of aerosols in the marine boundary layer to provide designers and users of electrooptics (EO) systems with parameters required to determine optimum system design and hence operational system limitations.

Measurements of the direct beam extinction coefficients (absorption plus single scatter) of optical frequencies through various continental type clouds, fogs, hazes and rain have been widely reported in the open literature. Recently, Bucher and Lerner [22] reported measurements of multiple scattering effects on 30 nsec pulses from a Q-switched ruby laser propagating through orographic clouds. The pulses received with varying FOV ( $1^\circ$  to  $4^\circ$ ) over a 6.4 km path varied between 1 and 10 usec in duration when there was a cloud in the propagation path. Quantitative measurements of the peak power losses as a function of receiver FOV were not addressed and detailed descriptions of the clouds (aerosol and hydrometer size distributions and their spatial variations) were not available.

It is the purpose of this test plan to define an experiment to measure the peak power losses and temporal characteristics as a function of FOV of optical pulses propagating through clouds (marine fogs). In addition to the propagation measurements the meteorological parameters describing the propagation path will be measured and used as inputs to computer codes to

assess the measured results and for propagation prediction purposes. Of primary interest here are those frequencies in the blue-green portion of the spectrum which after propagating through a cloud, can penetrate sea water and be of use as a submarine-to-aircraft satellite communications system.

Recently, the Naval Electronics Laboratory Center in collaboration with the Naval Research Laboratory initiated an experimental program to investigate the propagation of infrared ( $10.6 \mu$ ) radiation through optically thick clouds to assess the usefulness of heterodyne techniques for surface-to-satellite communications [2]. Unfortunately, this program was terminated just prior to data acquisition due to a recall of funds. Subsequent measurements were made over an 11-mile link transversing San Diego Bay and the results have been reported.[2] The instrumentation and experimental expertise developed for this program and other related laser radar projects are currently available for conducting the measurements proposed here. In addition, a unique multiremote sensing facility has been developed by NELC and is available for conducting the propagation parameter measurements. In the following sections the details of the test plan (site selection, facilities and instrumentation description, variables to be measured and schedule, theoretical background and results, and computer software capabilities) are presented.

## 2.0 THEORETICAL BACKGROUND AND PREDICTIONS

### 2.1 Introduction

The existence of clouds and fog in many regions of the earth presents a formidable problem to the designer of an optical communication system whose transmission channel is the atmosphere. These entities inhibit system performance by inducing beam spread, dispersion in angle-of-arrival, degradation of spatial coherence, and dispersion in time and frequency of the signal modulating the optical beam. Thus one is forced in many applications to accept receiver complexity and diminished data rates in return for nearly constant channel availability. The purpose of this section is to review the various theoretical formulations currently used to characterize optical propagation in single and multiple scattering media.

### 2.2 Mie Scattering and the Radiative Transfer Equations

The following discussion is a summary of the Radiative Transfer and Mie Scattering Theories taken from a review paper by Lerner and Holland [3]<sup>1</sup>.

#### 2.2.1 Radiative Transfer: Preliminary Considerations

The basis of classical transfer theory is the Lambert-Bouguer law, which states that the change in intensity of radiation due to an interaction with matter depends directly on both the incident intensity and the amount of matter. This linearity holds so long as the matter remains in the same physical state and/or if we consider quantities at a single frequency or wavelength. Thus a beam or pencil of radiation is attenuated by its interaction with the medium through which it passes. If the initial intensity is  $I$ , then after traveling a distance  $ds$  along the direction of propagation, the change in intensity will be<sup>2</sup>

$$\begin{aligned}
 dI &= -k_{\text{ext}}(s) \rho I ds \\
 &= -\beta_{\text{ext}}(s) I ds
 \end{aligned}$$

where

$\rho$  = density (g/cm<sup>3</sup>) of the attenuating medium

$k_{\text{ext}}$  = mass extinction coefficient (cm<sup>2</sup>/g)

$\beta_{\text{ext}}$  = volume extinction coefficient (cm<sup>-1</sup>)

In what follows, only the variations of intensity with respect to direction and spatial position will be indicated. The dependence on frequency, time, and other necessary parameters will nevertheless be understood unless otherwise stated.

The theory also assumes that emission by an element of mass or volume is linear in both intensity and the amount of matter present. The net increase in intensity in a distance  $ds$  along the direction of propagation is  $j(s)ds$ . The equation of radiative transfer for a given path through a medium can be thus expressed as

$$\frac{dI(s)}{ds} = -\beta_{\text{ext}}(s)I(s) + j(s) \quad (1)$$

Formal integration of this one-dimensional transfer equation of the path  $s = 0$  to  $s = T$  gives

$$I(s) = I(0)e^{-\tau} + \int_0^T j(s')e^{-(\tau-\tau')}ds' \quad (2)$$

in which the optical thickness along the path is  $\tau$

$$\begin{aligned}
 \tau &= \int_0^T \beta_{\text{ext}}(s)ds \\
 \tau' &= \int_0^{s'} \beta_{\text{ext}}(s'')ds''
 \end{aligned}$$

This formal solution to (1) shows that the resultant intensity is the sum of two distinct terms: the incident intensity attenuated by extinction along the path (0,T) and a component due to emission at points along the path, attenuated along that path (s',T). If we neglect the emission term, we have the usual form of the Lambert-Bouguer law. Thus we can define a "meteorological range" as the distance required to reduce the incident intensity to 2% of its original value: that is,

$$I(R)/I(0) = 0.02 = \exp \left\{ - \int_0^R \beta_{\text{ext}}(s) ds \right\}$$

or

$$\begin{aligned} R &\equiv \text{meteorological range} \\ &= 3.912 / \int_0^R \beta_{\text{ext}}(s) ds. \end{aligned}$$

This relation is widely used; however, it is deceptive in that the above describes nothing about the deposition of the light removed from the beam. That information is contained in the emission term. In general, the emission term consists of two distinct parts: (1) that due to the scattering of other radiation into the direction of interest, and (2) that due to true emission, e.g., thermal. Henceforth we will ignore this latter term, and consider only emission due to scattering.

Equations (1) or (2) are known as the "equation of radiative transfer". They serve to demonstrate the dependence of the classical theory on the scattering centers, or on the volume elements containing such scatters. Naturally, these volume elements should be small enough so they may be considered point sources of radiation; and the number of scatterers present in each volume not so large that multiple scattering effects are observed. Under these conditions, one is able to perceive a significant part of the physics behind the scattering phenomenon. It is possible to analyze multiple scattering problems with this formation, e.g., Dell-Imagine [4], but the mathematical and computational complexities increase significantly unless a modified computing technique, e.g., Dave and Gazdag [11] or a matrix approach, e.g., Plass, *et al.* [5], is utilized. For this development, we will limit ourselves to the single scattering problem.

In general, a medium may exhibit both scattering and absorption. Some of the energy removed from the beam will be scattered over all possible directions; the rest will be absorbed and lost to the radiation field. Thus we have

$$k_{\text{ext}} = k_{\text{sca}} + k_{\text{abs}}$$

where the subscripts denote scattering and absorption. An important auxiliary parameter is the "albedo for single scattering" defined to be

$$\omega_0 = \frac{k_{\text{sca}}}{k_{\text{ext}}} = \frac{k_{\text{sca}}}{k_{\text{sca}} + k_{\text{abs}}}, \quad 0 \leq \omega_0 \leq 1.$$

The mass scattering coefficient specifies the rate at which energy is scattered from the incident beam confined to solid angle  $d\omega$  by an element of mass  $dm$

$$\frac{dE}{dt} = \begin{cases} k_{sca} I dm d\omega \\ \omega_0 k_{ext} I dm d\omega \end{cases} \quad (3)$$

The distribution of the scattering energy is specified by the "scalar phase function"  $P(\gamma)$  where  $\gamma$  is the angle between the direction of incidence and the scattered direction. Thus, the rate at which energy is scattered into a solid angle  $d\Omega$  in a direction making an angle  $\theta$  with the direction of incidence of a beam of intensity  $I$  confined to a solid angle  $d\omega$  from an element of mass  $dm$  is

$$\frac{dE(\gamma)}{dt} = \begin{cases} k_{sca} I P(\gamma) \frac{d\Omega}{4\pi} d\omega dm \\ \omega_0 k_{ext} I P(\gamma) \frac{d\Omega}{4\pi} d\omega dm \end{cases} \quad (4)$$

The rate at which energy is lost from the beam due to scattering in all directions is

$$\begin{aligned} k_{sca} I dm d\omega \int_{\Omega} P(\gamma) \frac{d\Omega}{4\pi} \\ \omega_0 k_{ext} I dm d\omega \int_{\Omega} P(\gamma) \frac{d\Omega}{4\pi} \end{aligned} \quad (5)$$

It is apparent that equations (3) and (5) agree only if the scalar phase function is normalized to one over the unit sphere, i.e.,

$$\int \frac{P(\gamma)}{4\pi} d\Omega = 1.0.$$

These quantities completely specify the single scattering properties of an isotropic medium. For a more detailed treatment, see references [6], [7], and [8].

### 2.2.2 Single Particle Scattering Properties

The scattering and absorption properties of an isotropic, homogeneous sphere, illuminated by a plane monochromatic electromagnetic wave, can be described completely by the well-known Mie theory [9-11]. We will only give a brief description here.

Essentially, given a diameter  $D$  of the spherical particle, its complex refractive index relative to the surrounding medium  $\tilde{m}$  and the wavelength  $\lambda$  of the incident plane wave, the theory yields the dimensionless complex scattering amplitudes for any direction  $\theta$  from the direction of incidence. The expressions have their simplest form when the electric vector of both incident and scattered waves are resolved into components (1) perpendicular, and (2) parallel to the plane of scattering; that is, the plane defined by the directions of incidence and scattering. Figure 1 depicts the geometry of the problem for a particular incident polarization. The scattering amplitudes are then

$$S_1(\tilde{m}, x, \theta) = \sum_{n=1}^{\infty} \frac{2n+1}{n(n+1)} [a_n(\tilde{m}, x) \pi_n(\theta) + b_n(\tilde{m}, x) \xi_n(\theta)]$$

$$S_2(\tilde{m}, x, \theta) = \sum_{n=1}^{\infty} \frac{2n+1}{n(n+1)} [a_n(\tilde{m}, x) \xi_n(\theta) + b_n(\tilde{m}, x) \pi_n(\theta)].$$

The quantities  $a_n(\tilde{m}, x)$  and  $b_n(\tilde{m}, x)$  are the Mie scattering coefficients, which are certain Ricatti-Bessel functions of real and complex argument.  $\pi_n(\theta)$  and  $\xi_n(\theta)$  are spherical harmonics expressible as Legendre polynomials. The quantity  $x$  is called the normalized Mie-size parameter and is given by

$$x = \frac{\pi D}{\lambda}.$$

The components of the scattered intensity resolved in the directions perpendicular and parallel to the scattering plane are

$$i_1(\tilde{m}, x, \theta) = |S_1(\tilde{m}, x, \theta)|^2$$

$$i_2(\tilde{m}, x, \theta) = |S_2(\tilde{m}, x, \theta)|^2$$

The intensity scattered by the sphere in any direction, assuming unpolarized incident light, is the average over all possible orientations of the incident electric vector or

$$I_s(\tilde{m}, x, \theta) = \frac{I_0}{2k^2} [i_2 + i_1]$$

in which  $k$  is the propagation constant,  $k = 2\pi/\lambda$ , and  $I_0$  is the incident flux.



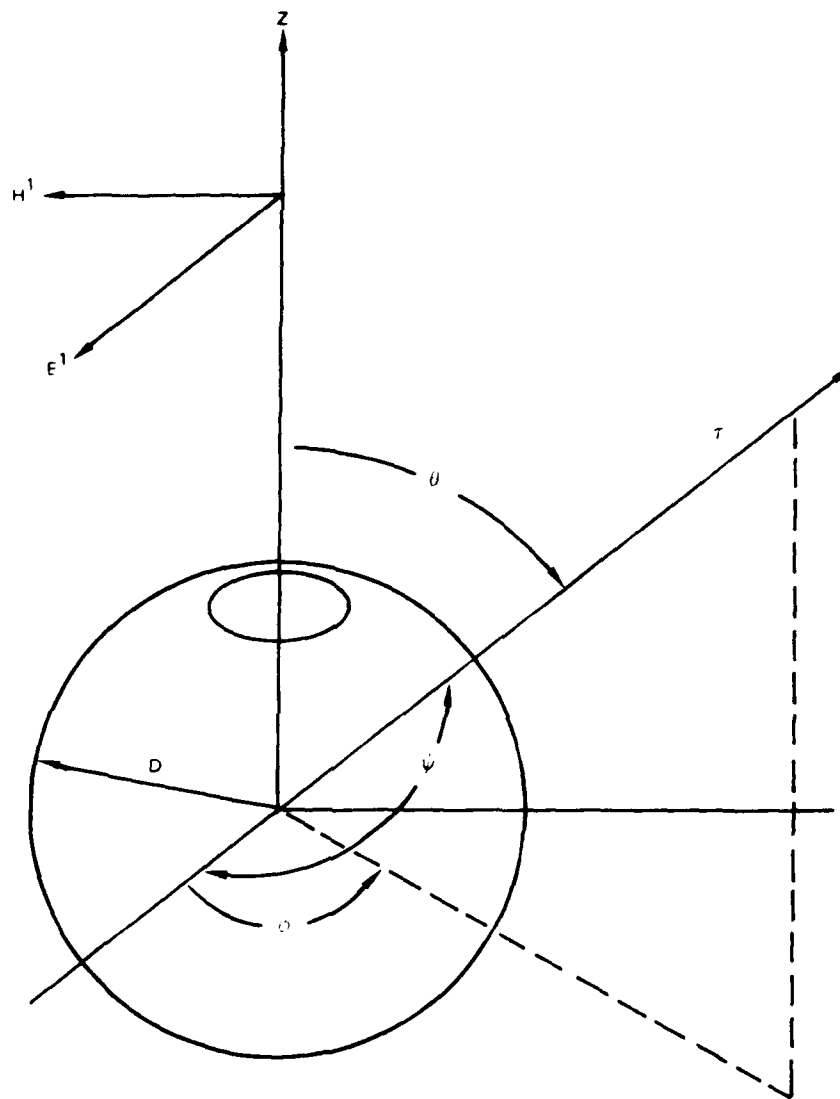


Figure 1. Geometry for scattering from a spherical particle with radius  $D$ . The vector  $r$  represents the direction of the outgoing wave resulting from an encounter of an incident wave with the polarization shown traveling along the positive  $Z$  axis with the particle.

The total extinction and scattering cross sections  $\sigma_{\text{ext}}$  and  $\sigma_s$  can also be expressed in terms of the Mie coefficients

$$\begin{aligned} Q_{\text{ext}}(\tilde{m}, x) &= \frac{4}{\pi D^2} \sigma_{\text{ext}}(\tilde{m}, x) \\ &= \frac{2}{x^2} \sum_{n=1}^{\infty} (2n+1) \operatorname{Re} \left\{ a_n + b_n \right\} \\ Q_s(\tilde{m}, x) &= \frac{4}{\pi D^2} \sigma_s(\tilde{m}, x) \\ &= \frac{2}{x^2} \sum_{n=1}^{\infty} (2n+1) \left\{ |a_n|^2 + |b_n|^2 \right\}. \end{aligned}$$

The notation  $\operatorname{Re}$  denotes the real part of the complex quantity in the brackets, while  $Q_{\text{ext}}$  and  $Q_s$  are the extinction and scattering efficiencies defined as the corresponding cross sections normalized by the cross sectional area of the sphere.

The true absorption efficiency (cross section) is defined to be

$$Q_{\text{abs}}(\tilde{m}, x) = Q_{\text{ext}} - Q_s.$$

Thus for nonabsorbing dielectric spheres, the scattering and extinction coefficients are equal. The scalar phase function for a single particle is

$$\frac{P(\gamma)}{4\pi} = \frac{1}{2\pi x^2 Q_s} \begin{bmatrix} 1 & +1 \\ 1 & 2 \end{bmatrix}$$

and is obviously normalized to one.

For an element of volume containing a number  $N$  of identical spherical particles, the volume scattering across section is simply

$$\beta_s(\tilde{m}, x) = \sigma_s N = \frac{\pi D^2}{4} N Q_s$$

with dimensions of  $\text{cm}^2/\text{cm}^3$  or  $\text{cm}^{-1}$ . The differential volume scattering coefficient is

$$\beta_s(\bar{m}, x, \theta) = N \sigma_s(\bar{m}, x, \theta) = \frac{N}{2K^2} [i_2(\bar{m}, x, \theta) + i_1(\bar{m}, x, \theta)]$$

and the scalar phase function for the volume element is

$$\begin{aligned} \frac{P(\gamma)}{4\pi} &= \frac{\beta_s(\bar{m}, x, \theta)}{\sigma_s(\bar{m}, x)} \\ &= \frac{1}{2-x^2 Q_s(\bar{m}, x)} [i_2(\bar{m}, x, \theta) + i_1(\bar{m}, x, \theta)] \end{aligned}$$

which is identical to the phase function for a single particle. The phase function is independent of the amount of scattering material in the volume and depends only on the particle size parameter  $x$  and the refractive index  $\bar{m}$  (assuming that the volume does not contain so many particles that multiple scattering effects appear).

As one might imagine, the scalar phase function plays a significant role in single (and also multiple) scattering problems. In fact, much work has been done to determine under what conditions the entire Mie series is not required and/or can be replaced by some analytical expression [5,9,12,13]. We will find evidence of this quest in a later subsection concerned with pulse propagation through a multiple scattering medium.

### 2.2.3 Elements of Radiative Transfer Theory

Once the relevant single scattering properties are known, it is possible to write down the emission coefficient explicitly. Consider a cylindrical element of volume (figure 2) characterized by a volume extinction coefficient  $\beta_{\text{ext}}$ , a scalar phase function, and an albedo for single scattering  $\omega_0$ . Assuming the volume has a base area  $dA$  and a height  $dz$ , consider a beam of intensity  $I$  contained in a solid angle  $d\omega'$  that is incident on the top surface of the volume at an angle  $\theta'$  from the surface normal and at an azimuthal angle  $\phi'$  from a reference plane through the normal. The amount of energy entering the volume in unit time is

$$I(\theta', \phi') d\omega' dA \cos \theta'$$

and the path through the volume is

$$dz \sec \theta'.$$

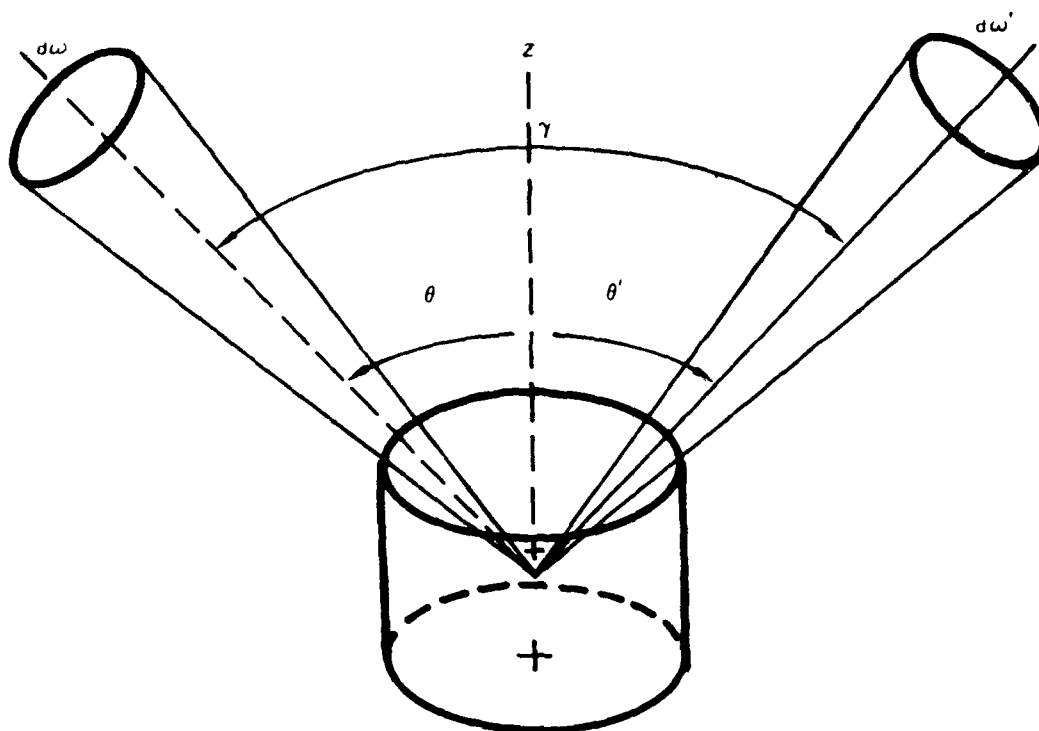


Figure 2. Volume scattering geometry.[1].

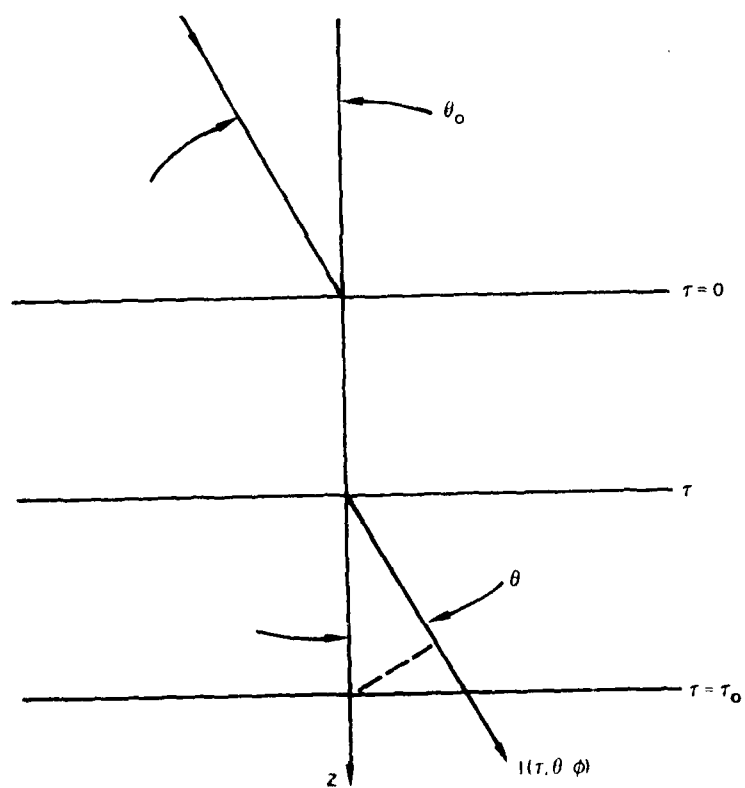


Figure 3. Radiative transfer geometry.[3].

The energy lost from the beam in unit time is

$$\beta_{\text{ext}} I(\theta', \phi') dA \cos \theta' d\omega' dz \sec \theta'$$

or

$$\beta_{\text{ext}} I(\theta', \phi') d\omega' dAdz.$$

(6)

Of this energy, a fraction  $\omega_0$  will be lost due to scattering by the volume. The scattered energy will be distributed over directions  $(\theta, \phi)$  into solid angle  $d\omega$  according to the phase function  $P(\gamma)$  where  $\gamma$  is the angle between directions  $(\theta', \phi')$  and  $(\theta, \phi)$ . The energy per unit time interval that is scattered into the solid angle  $d\omega$  from the volume element  $dV = dAdz$  will be

$$\omega_0 \beta_{\text{ext}} I(\theta', \phi') \frac{P(\gamma)}{4\pi} d\omega d\omega'.$$

The emission coefficient  $j_s$  is defined as the amount of energy per unit time interval emitted by an element of volume in a given direction. By integrating over all possible incident angles  $(\theta', \phi')$  we have

$$j_s(\theta, \phi) dV d\omega dt = \omega_0 dV d\omega dt \frac{\beta_{\text{ext}}}{4\pi} \int_{\omega'} P(\gamma) I(\theta', \phi') d\omega'. \quad (7)$$

The source function for an elemental volume is defined to be

$$\beta_{\text{ext}}^{-1} S(\theta, \phi) = j_s(\theta, \phi).$$

Let us now use these latter two quantities to solve the equation of transfer in more detail. Figure 3 depicts the problem's geometry. A plane-parallel homogeneous and isotropic medium is illuminated from a direction  $(\theta_0, \phi_0)$  relative to the surface normal by plane-wave irradiance of  $\pi F$  watts/cm<sup>2</sup>. Since we are assuming the medium to be homogeneous and isotropic, the single scattering properties are independent of position inside the medium, but the intensity, i.e., source function, depends on depth of penetration and on direction. It is convenient to use a normalized optical thickness defined as

$$d\tau = \beta_{\text{ext}} dz$$

as the depth variable. Thus, along any incremental path  $ds$  inside the slab structure making an angle  $\theta$  to the normal, we have

$$ds = dz \sec \theta = \frac{d\tau}{\beta_{\text{ext}}} \sec \theta.$$

This implies we can write the equation of transfer as

$$\cos \theta \frac{dI(\tau, \theta, \phi)}{d\tau} = -I(\tau, \theta, \phi) + \beta(\tau, \theta, \phi).$$

The intensity field  $I(\tau, \theta, \phi)$ , as you recall, is composed of two distinct parts: the incident intensity, attenuated by the extinction processes incurred along the path of propagation, and a diffuse intensity due to scattering and true emission. Here, we again chose to ignore true emission, and consider only scattering-based emission. Therefore, let us write the source function as the sum of two terms

$$B(\tau, \theta, \phi) = B_s(\tau, \theta, \phi) + B_o(\tau, \theta, \phi),$$

where  $B_s(\tau, \theta, \phi)$  denote the source function due to scattering into direction  $(\theta, \phi)$  of the diffuse intensity field incident on the volume element located at optical depth  $\tau$ .  $B_o(\tau, \theta, \phi)$  is the source function due to the scattering of the incident radiation by the volume element from the direction  $(\theta_o, \phi_o)$  into  $(\theta, \phi)$ . Mathematically, it follows from equations (6) and (9) that

$$B_s(\tau, \theta, \phi) = \frac{\omega_o}{4\pi} \int_0^{2\pi} \int_0^\pi P(\nu) I(\tau, \theta, \phi') \sin \theta' d\theta' d\phi'$$

where  $I(\tau, \theta, \phi)$  denotes the diffused intensity.

The direction source function  $B_o(\tau, \theta, \phi)$  comes above as follows: Initially it was assumed that the incident irradiance of  $\pi F$  watts/cm<sup>2</sup> illuminated the planar structure at angle  $(\theta_o, \phi_o)$ . The irradiance reaching an optical depth  $\tau$  along a path inclined at an angle  $\theta_o$  to the normal axis of the structure is

$$\pi F \exp \left\{ -\tau \sec \theta_o \right\}.$$

Thus we have

$$B_o(\tau, \theta, \phi) = \omega_o \frac{P(\gamma_o)}{4} F \exp \left\{ -\tau \sec \theta_o \right\} \quad (8)$$

with  $\gamma_0$  being the angle between  $(\theta_0, \phi_0)$  and  $(\theta, \phi)$ . This implies

$$B(\tau, \theta, \phi) = \frac{\omega_0}{4\pi} \int_0^{2\pi} \int_0^\pi I(\tau, \theta', \phi') P(\gamma) \sin \theta' d\theta' d\phi' + \frac{\omega_0}{4} P(\gamma_0) F \exp \left\{ -\tau \sec \theta_0 \right\} \quad (9)$$

where  $P(\gamma) = P(\theta, \phi, \theta', \phi')$ . One need only apply the appropriate boundary condition in order to complete the solution to the problem.

### 2.3 Mutual Coherence Function

In the above analysis, we regarded radiation transfer purely as a collection of photons diffusing through a scattering medium. This is sometimes a dangerous oversimplification of the problem as one has neglected to investigate the evolution of the radiation field's coherence. One finds in practice that signal coherence can affect the performance of communication system significantly, e.g., a loss of spatial and temporal coherence in a heterodyne system can cause channel fading. Thus one recognizes propagation through single- and multiple-scattering media to be a stochastic process.

Stochastic processes are generally analyzed in terms of their statistical moments [14,15]. Probably the most important statistical moment is the second order moment; this is because of the relative ease in which it can be handled both mathematically and experimentally. One finds that many of the theoretical studies concerned with scattering media utilized this technique. For example, Heggstad [19] derived a generalized scattering function from this moment for his paper on optical communications through multiple-scattering media. Ishimara [14], on the other hand, used the two frequency mutual coherence function (second order statistical moment of the field) in his analysis. Livingston [17] and Lutomirski [18] were both successful in developing a generalized mutual coherence analysis of multiple-scattering effects on optical propagation. Since all of the papers are based on the same relative formulation, we will describe only Livingston's work and leave it to the reader to investigate the other variations cited.

#### 2.3.1 Derivation of the Radiation Transport Equation

Consider a semi-infinite slab of scattering medium with faces perpendicular to the axis of a coordinate system. Let the slab have finite thickness in the  $Z$  direction. The radiant intensity  $S(\underline{r}, \hat{n})$  is conventionally defined as the flux of energy through a unit area in unit time  $dt$  moving in the mean direction denoted by the direction vector  $\hat{n}$ . That is

$$dE \text{ joules} = dA S(\underline{r}, \hat{n}) d\hat{n} dt \quad (10)$$

or

$$S(\underline{r}, \hat{n}) = dE/dAd\hat{n}dt \text{ watts/m}^2 \cdot \text{ster}, \quad (11)$$

where  $dA$  is an element of area and

$$d\hat{n} = \sin \theta \, d\theta \, d\phi \quad (12)$$

is an element of solid angle. Equation 11 defines a pencil of radiation introduced by Chandrasekhar [8]. As an elementary area of a wavefront  $dA$  moves with the wave at velocity  $c$ , it sweeps out a volume as shown in fig 4. During this passage radiant energy may be gained or lost, depending on whether energy is scattering into the volume moving parallel to  $\hat{n}$  or lost to it by extinction. The radiative transfer equation then represents a balance of gains and losses during this process. For the moment, we will suppress the dependence of the cross sections on particle size and refractive index. For polydisperse systems average radiation transfer is obtained by summing over all particle sizes. Let  $n$  be the number of scattering centers per cubic meter and  $\sigma_{\text{ext}}$ ,  $\sigma_{\text{sca}}$  and  $\sigma_{\text{abs}}$  be the total extinction cross section, total scattering cross section, and total absorption cross section, respectively, defined in the previous section. Assuming no shadow effects, the fraction of the elementary area covered by scatterers is

$$\text{fraction} = \sigma_{\text{ext}} n(\hat{n} \cdot \hat{Z})c \, dt. \quad (13)$$

Therefore the loss to the radiant energy due to extinction is given by multiplying Eq. 13 by  $S \, dAd\hat{n}dt$  to give

$$d^2E_{\text{loss}} = [\sigma_{\text{ext}} n(\hat{n} \cdot \hat{Z})c \, dt](S \, dAd\hat{n}dt). \quad (14)$$

Similarly, radiation scattered into the volume moving in the direction  $\hat{n}$  is given by

$$d^2E_{\text{gain}} = \sigma_{\text{sc}} n(\hat{n} \cdot \hat{Z})c \, dt \frac{1}{4\pi} \int P(\hat{n}, \hat{n}') S(\underline{r}, \hat{n}') d\hat{n}' dAdt. \quad (15)$$

Here,  $P$  is the probability of scattering radiation from direction  $\hat{n}'$  to direction  $\hat{n}$ . The net change, gain minus loss, is just equal to the substantial derivative of  $E$ , namely,  $(dE/dt)dt$ . For steady-state conditions

$$dt \frac{d^2E}{dt} = \frac{dr}{dt} \cdot \nabla E dt = c\hat{n} \cdot \nabla S \, dAd\hat{n}(\hat{n} \cdot \hat{Z})dt, \quad (16)$$

where the defining equation for  $S$  has been used and also the fact that the wave moves with the speed of light  $c$ . Thus the equation satisfied by  $S$ , namely

$$\hat{n} \cdot \nabla S(\underline{r}, \hat{n}) = -\sigma_{\text{ext}} n S(\underline{r}, \hat{n}) + \frac{n\sigma}{4\pi} \int P(\hat{n}, \hat{n}') S(\underline{r}, \hat{n}') d\hat{n}', \quad (17)$$



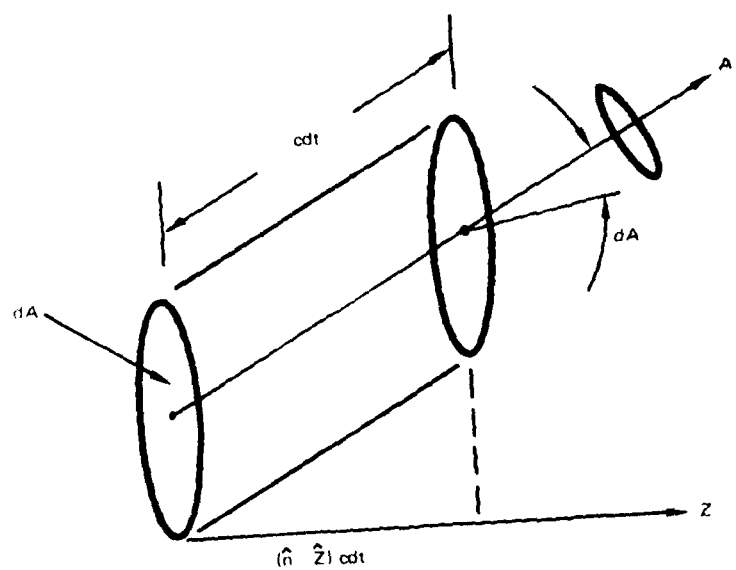


Figure 4 Volume swept out by an elementary area of a wavefront moving in the direction  $\hat{n}$  in time  $dt$ . The volume  $V = dA(\hat{n} \cdot \hat{Z}) cdt$ .

is the standard radiation transport expression. In the preceding, a slightly more general expression follows if we allow  $S$  to depend on the light frequency  $\omega$ , as would be required if Doppler-scattering is of interest:

$$\hat{n} \cdot \nabla S(\underline{r}, \hat{n}, \omega) + n \sigma_{\text{ext}} S(\underline{r}, \hat{n}, \omega) = \frac{n \sigma_{\text{sc}}}{4\pi} \int_{-\infty}^{\infty} d\omega' \int \underline{P}(\hat{n}, \hat{n}', \omega - \omega') S(\underline{r}, \hat{n}', \omega') d\hat{n}'. \quad (18)$$

Apart from differences in notation and a more complex kernel, this equation is identical with Fante's [19]. Either Eq. 17 or Eq. 18 along with an expression for  $\underline{P}$  serve to define the evolution of the radiant intensity  $S$  through the cloud. Since  $\underline{P}$  can be expressed in a series of Legendre polynomials, Eq. 18 can be numerically treated as an infinite set of coupled differential equations or, what is equivalent, a set of homogeneous algebraic equations to be solved by matrix inversion. Before considering the relationship of  $S$  to quantities of interest, let us rewrite Eq. 17 as follows:

$$\frac{\partial}{\partial \tau} S(p, \tau, \hat{n}) + \frac{n_{\perp}}{n \sigma_{\text{ext}}} \cdot \nabla_{\perp} S(p, \tau, n_{\perp}) + S(p, \tau, n_{\perp}) = \frac{\omega_0}{4\pi} \int dn_{\perp} \underline{P}(n_{\perp}, n'_{\perp}) S(p, \tau, n'_{\perp}), \quad (19)$$

where the optical depth  $\tau$  is given by

$$\tau = n \sigma_{\text{ext}} Z$$

and the albedo for scattering

$$\omega_0 = \sigma_s / \sigma_{\text{ext}} \leq 1$$

has been introduced. In the notation of Eq. 19,  $n_{\perp}$  is the perpendicular direction to  $Z$ . Further progress in analyzing Eq. 19 can be made if  $S$  depends on  $\tau$  and the central angle alone, that is, if  $S$  is homogeneous in planes transverse to  $Z$ , or  $\underline{P}$  depends only on the difference of the vectors  $n_{\perp}$  and  $n'_{\perp}$ . The former case is fully considered in Chandrasekhar's work, and the latter, termed small angle scattering approximation, is considered by Fante in Ref. 17. Let us define

$$F(\underline{k}, \underline{p}, \tau) = (2\pi)^{-4} \iiint S(\underline{r}, \underline{n}_{\perp}, \tau) e^{i \underline{k} \cdot \underline{r} + i \underline{p} \cdot \underline{n}_{\perp}} d\tau d\underline{n} \quad (20a)$$

and

$$Q(\mathbf{p}) = (2\pi)^{-2} \iint d\mathbf{n}_\perp P(\mathbf{n}_\perp) e^{i\mathbf{p} \cdot \mathbf{n}_\perp}, \quad (20b)$$

where it is now assumed that

$$P(\mathbf{n}_\perp, \mathbf{n}'_\perp) = P(\mathbf{n}_\perp - \mathbf{n}'_\perp). \quad (20c)$$

The equation satisfied by  $F$  is a combination of Eqs. 19, 20a, and 20b, and the result is

$$\frac{\partial F}{\partial \tau}(\mathbf{k}, \mathbf{p}, \tau) + F(\mathbf{k}, \mathbf{p}, \tau) - \frac{i\mathbf{k} \cdot \mathbf{n}_\perp}{n\sigma} F(\mathbf{k}, \mathbf{p}, \tau) - \pi\omega Q(\mathbf{p}) F(\mathbf{k}, \mathbf{p}, \tau) = 0. \quad (21)$$

The solution of the first-order equation in the optical depth is readily effected:

$$F(\mathbf{k}, \mathbf{p}, \tau) = F(\mathbf{k}, \mathbf{p}, 0) e^{-\tau} e^{(i\mathbf{k} \cdot \mathbf{n}_\perp / n\sigma) + \pi\omega Q(\mathbf{p}) \tau}. \quad (22)$$

The inverse transform of this equation yields the solution for  $S$ :

$$S(\mathbf{r}, \mathbf{n}_\perp, \tau) = e^{-\tau} \iiint F' \left( \mathbf{k}, \mathbf{p} + \frac{\mathbf{k}\tau}{n\sigma_{\text{ext}}}, 0 \right) e^{-i\mathbf{k} \cdot \mathbf{r} - i\mathbf{p} \cdot \mathbf{r}_\perp + \pi\omega Q(\mathbf{p}) \tau} d\mathbf{p} d\mathbf{k}. \quad (23)$$

Here,  $F'(\mathbf{k}, \mathbf{p}', 0)$  is the transform of the initial radiance distribution, and it remains only to specify  $Q(\mathbf{p})$  to obtain an explicit solution. Given an initial field  $u(\mathbf{r})$ , then, the initial transformed irradiance distribution can be written

$$F(\mathbf{k}, \mathbf{p}, 0) = (2\pi)^{-4} \iint e^{i\mathbf{k} \cdot \mathbf{r}} u(\mathbf{r} + \mathbf{p}/2k_0) u^*(\mathbf{r} - \mathbf{p}/2k_0) d\mathbf{r}, \quad (24)$$

where  $k_0$  is  $2\pi/\lambda$ . A similar expression holds for any value of  $\tau$  and, when averaged over a suitable ensemble, is related to the mutual coherence. Thus

$$\begin{aligned} \Gamma(\mathbf{R}, \mathbf{p}, \tau) &= \langle u(\mathbf{r}_1, \tau) u^*(\mathbf{r}_2, \tau) \rangle \\ &= (2\pi)^2 \iint F(\mathbf{k}, \mathbf{k}_0, \tau) e^{i\mathbf{k} \cdot \mathbf{R}} d\mathbf{k} \\ &= (2\pi)^2 \iint F_0 \left( \mathbf{k}, \mathbf{k}_0 + \frac{\mathbf{k}\tau}{n\sigma_{\text{ext}}}, 0 \right) e^{-\tau - i\mathbf{k} \cdot \mathbf{R} + \pi\omega Q(\mathbf{k}_0) \tau} d\mathbf{k} \end{aligned} \quad (25)$$

The last expression follows after the substitution of the solution, Eq. 22, into the second line. It is a mutual coherence function, defined in Eq. 25, that is central to both a description of the propagation process and to the carrier-to-noise calculation of the optical heterodyne communication system. In Eq. 25,  $\mathbf{R}$  is the center-of-mass vector in the receiver plane (perpendicular to the axis of propagation) and  $\rho$  is the difference vector in the same plane:

$$\mathbf{R} = \frac{1}{2} (\mathbf{r}_1 + \mathbf{r}_2)$$

and

$$\rho = \mathbf{r}_1 - \mathbf{r}_2,$$

where  $\mathbf{r}_1$  and  $\mathbf{r}_2$  are two-dimensional vectors in the receiver plane. Let the launched beam have the form

$$u(\mathbf{r}) = u_0 e^{-(\pi^2/2A_0) + (ik_0 r^2/2R_0)}, \quad (26)$$

where  $A_0$  is the effective aperture area and  $R_0$  is the radius of curvature of the launched wavefront. (A collimated beam is given by  $R = -\infty$ .) Combining Eqs. 22 and 20 leads to

$$F_0 \left( \mathbf{k}_1 \rho + \frac{k_1 \tau}{n \sigma_{\text{ext}}} \right) = \frac{A_0 |u_0|^2}{(2\pi)^4} e^{-(R_1 k^2 + \beta_2 \rho^2 + \beta_3 \mathbf{k} \cdot \rho)}, \quad (27)$$

where

$$\begin{aligned} \beta_1 &= \frac{A_0}{4\pi} + \left( \frac{\pi}{4k_0^2 A_0} + \frac{A_0}{4\pi R_0^2} \right) z^2 + \frac{A_0}{2\pi R_0} z, \\ \beta_2 &= \frac{\pi}{4k_0^2 A_0} + \frac{A_0}{4\pi R_0^2}, \\ \beta_3 &= 2z \left( \frac{\pi}{4k_0^2 A_0} + \frac{A_0}{4\pi R_0^2} \right) + \frac{A_0}{2\pi}. \end{aligned}$$

Substitution of Eq. 27 into the expression for  $\Gamma$  leads to

$$\Gamma(\mathbf{R}, \rho, \tau) = \frac{A_0 |u_0|^2}{4\pi^2} e^{-\tau \beta_2 k_0^2 \rho^2} \int e^{-\beta_1 k^2 - \beta_3 \mathbf{k} \cdot \rho - i \mathbf{k} \cdot \mathbf{R}} \pi \omega Q(\mathbf{k}_0 \rho) \tau \, d\mathbf{k} \quad (29)$$

The integral over  $k$  can be carried out to give

$$\Gamma(R, \rho, \tau) = \frac{A_o |u_o|^2}{4\pi\beta_1} e^{-\tau - (R^2/4\beta_1) - [\beta_2 - (\beta_3^2/4\beta_1)] k_o^2 \rho^2 + \pi\omega Q(k_o \rho)\tau} \cos(\beta_3 k_o R \rho / 2\beta_1) . \quad (30)$$

For a collimated beam centered at  $R = 0$

$$\Gamma(0, \rho, \tau) = \frac{A_o |u_o|^2}{A_o + \frac{\pi^2 Z^2}{k_o^2 A_o}} e^{-\tau - [\rho^2/4(A_o/\pi + \pi Z^2/k_o A_o)] + \pi\omega Q(k_o \rho)\tau} . \quad (31a)$$

If we further assume that the receiver is in the far field of the transmitter aperture, we can write out a simple expression for the normalized mutual coherence function:

$$\gamma(0, \rho, \tau) = e^{-(k_o^2 A_o \rho^2 / 4\pi Z^2) + \pi\omega Q(k_o \rho)\tau} . \quad (32a)$$

#### 2.4 Monte Carlo Computer Simulation

Monte Carlo computer simulation can be applied to any problem if one knows the probability for each step in a sequence of events and desires the probability of the total of all possible events. Many researchers, most notably Bucher [12], and Plass and Kattawar [18], have contributed significantly to the area of laser irradiance through single- and multiple-scattering media using this technique. The advantages of this method are the following [20]:

(1) The calculation may be performed for any single scattering function regardless of the degree of anisotropy.

(2) Any relevant parameter such as the single scattering albedo, number density of molecular and aerosol scattering centers, and the various cross sections may be varied with optical depth in the atmosphere in any desired fashion.

(3) The radiation reflected by the boundary interface may follow any desired distribution.

(4) Any reasonable number of polar and azimuthal angles may be selected.

(5) The average mean optical path of both the reflected and transmitted photon may be easily calculated.

The disadvantage of the Monte Carlo method is twofold: First, the standard deviation of the results is roughly inversely proportional to the square root of the computing times. Therefore this technique may not be practical if a high degree of accuracy is required. Second, this technique does not lend insight into the physics of the process nor does it immediately provide the functional dependencies required for parameter variation.

The purpose of this section is to review the Monte Carlo method in more detail utilizing a representative paper, reference [12] by E. A. Bucher to be exact.

#### 2.4.1 The Method

A Monte Carlo Computer simulation is essentially a calculation based on some mathematical model of a physical situation. We will now describe the model and technique Bucher employed in his analysis.

The configuration chosen for the multiple scattering medium was a plane-parallel slab of infinite width and physical thickness  $T$ . The medium itself was assumed to be homogeneous and isotropic in nature. The above structure was chosen for its mathematical simplicity.

Figure 5 depicts a typical propagation path simulation. A normally incident ray travels a distance  $d_1$  until it is scattered the first time. On scattering a new direction  $(\theta_1, \phi_1)$  is selected relative to the incident ray. The ray then travels a distance  $d_2$  to its second scattering. At each successive scattering, a new direction  $(\theta_i, \phi_i)$  relative to the incident normal is chosen. Then, the ray travels a distance  $d_{i+1}$  to the next scattering event. This process continues until the ray leaves the scattering medium by either of its two planar boundaries. Rays leaving through the top (incident) boundary are indicative of back-scattered irradiance. Rays exiting the bottom boundary indicate the transmitted light. For each of these latter rays, the computer program records its total travel distance, exit angle, and radius of the exit point relative to the straight-through axis. This information was used later to calculate several statistical measures after a sufficient number of propagation paths had been traced.

The distance  $d_j$  that a ray travels in going from the  $(j-1)^{th}$  scatterer to the  $j^{th}$  scatterer was set up by Bucher to be randomly selected from a probability density

$$P(d_j) = \left(\frac{1}{D}\right) \exp \{-d_j/D\} ;$$

That is, the random variable  $d$  was chosen to assume values between  $d$  and  $d+\Delta d$  with total probability  $(1/D) \exp \{-d/D\} \Delta d$ . The quantity  $D$  is the scaling parameter of the exponential and is also the average value of the random variable  $d$ .

The scattering angle  $\theta_j$  and  $\phi_j$  are selected independently for each scattering event. The angles  $\theta$  and  $\phi$  represent the polar and rotation angles, respectively, in a spherical coordinate system whose origin is in the direction of the incident ray. In this configuration,  $\theta$  is the angle between the incident and scattered rays in the plane of scattering; and  $\phi$  is the rotation of the scattering plane about the incident ray. At each scattering,  $\phi$  was randomly selected from all possible values of  $\phi$  between 0 and  $2\pi$ . This uniform distribution for the rotation angle can be justified either on the basis of spherical scatterers, or on the basis of arbitrarily shaped scatterers, with no preferred spatial orientation.

Selection of the  $\theta$ -angle distribution, i.e., scalar phase function, involves the particular scattering mechanism of the medium and raises both physical and computational questions. As noted before, we will return to this question in the section on pulse propagation through multiple scattering media.

#### 2.4.2 The $\theta$ -angle Distribution Function

During our discussion of Monte Carlo computer simulation, we stated that the choice of the  $\theta$ -angle distribution function involved the particular scattering mechanism of the medium modeled and thus raised both physical and computational questions. Bucher responded to this situation by using two approximate scattering functions in conjunction with the full Mie series scattering function in his analysis and then comparing their results. The two approximating functions chosen were the megaphone and the Henyey-Greenstein functions. As it turned out, Bucher found good agreement between all three scattering functions for diffusion thicknesses greater than 3. The diffusion thickness is a weighted optical thickness and is defined to be

$$\tau_d = (1 - \langle \cos \theta \rangle) T/D$$

where

$T$          $\equiv$  physical thickness of the medium

$D$          $\equiv$  usual mean-free path between scatterings

$\langle \cos \theta \rangle$   $\equiv$  average cosine of the scattering angle relative to the incident direction

The wavelength used in the analysis was  $.7\mu$  and the particles were assumed to have a refractive index of 1.34 and a radius distribution between  $3.8\mu$  and  $4.8\mu$ .

## 2.5 Theoretical Results

### 2.5.1 Multipath Propagation Parameters [4,12,16,20-23]

If a collimated optical pulse is incident on a multiple-scattering region, the beam will experience beam spreading, dispersion in angle of arrival, attenuation, degradation of spatial coherence, and dispersion in time and frequency of the signal modulating it after transversing the region. These effects are related to the following multipath propagation parameters.

- a. angular spreading
- b. spatial spreading
- c. multipath time spreading
- d. total transmission
- e. Doppler spreading

Figure 6 illustrates a few of these parameters graphically. We have omitted polarization spreading as Bucher chose not to include it in the simulation.

"Angular spreading" constitutes an effective decollimation of the incident radiation. It contributes to beam spread, dispersion in angle-of-arrival, and loss of spatial coherence.

"Spatial spread," on the other hand, indicates the dimensional increase of the beam's finite cross section. It is related to the above parameter in that angular spread inside the medium produces a spatial spreading as the pulse propagates on. Spatial coherence and beam spread are related to this parameter.

Different distances along the various possible propagation paths imply different transit times for a photon. Thus, a short optical pulse will incur pulse broadening after transversing a multiple scattering region. Communication theorists often refer to this effect as "multipath time spreading" and denote its counterpart parameter by the letter  $L$  and the same name [21,25]. One finds that this quantity is very important in communication applications in that  $1/L$  represents the maximum pulse frequency which can be resolved.

"Total transmission" describes the amount of irradiance left in the pulse after transversing the medium. It is directly related to the beam attenuation.

If the scatters in the medium are moving, one finds that a change in the wavelength (frequency) of the light will occur after each scattering event. This wavelength change is called a "Doppler shift." If these scatters are also in relative motion to one another, the total Doppler shift incurred along the various scatter paths will be different. Hence, the irradiance transmitted through the scattering region from a single frequency source will contain a range of "Doppler spread" frequencies. We will ignore this parameter in the present discussion since current optical receivers fail to possess both the selectivity and the sensitivity necessary to measure this effect.



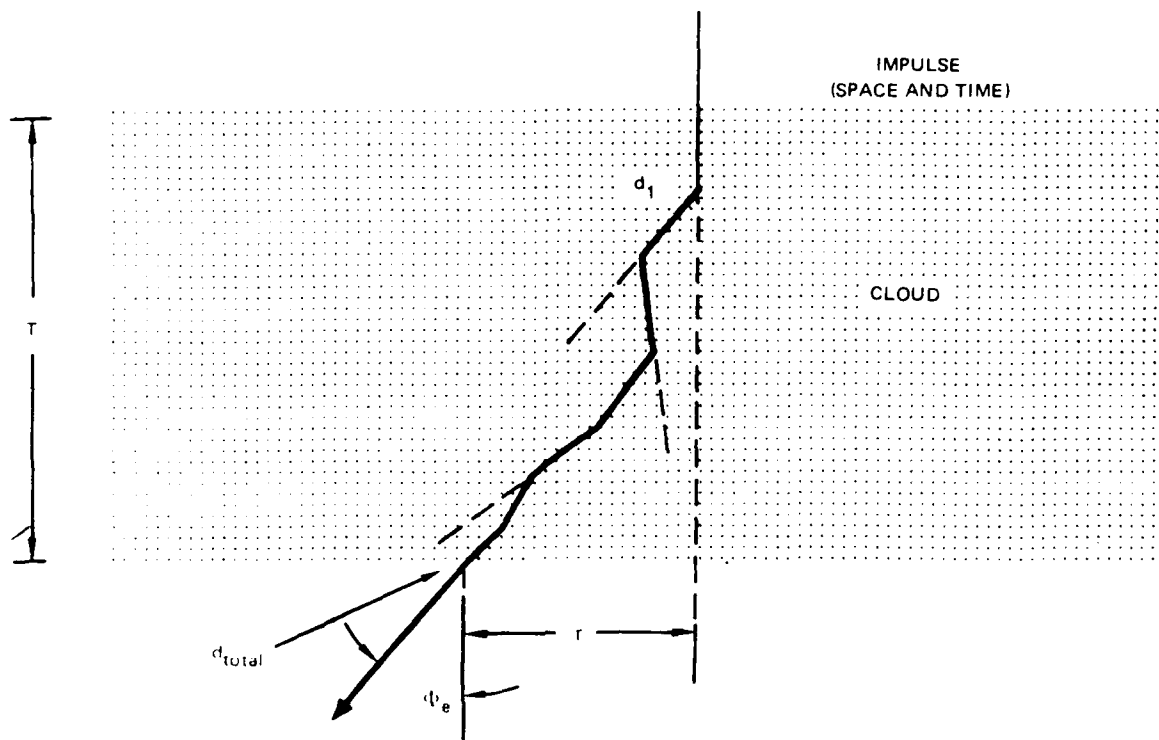


Figure 5. Simulation parameters and measures [10].

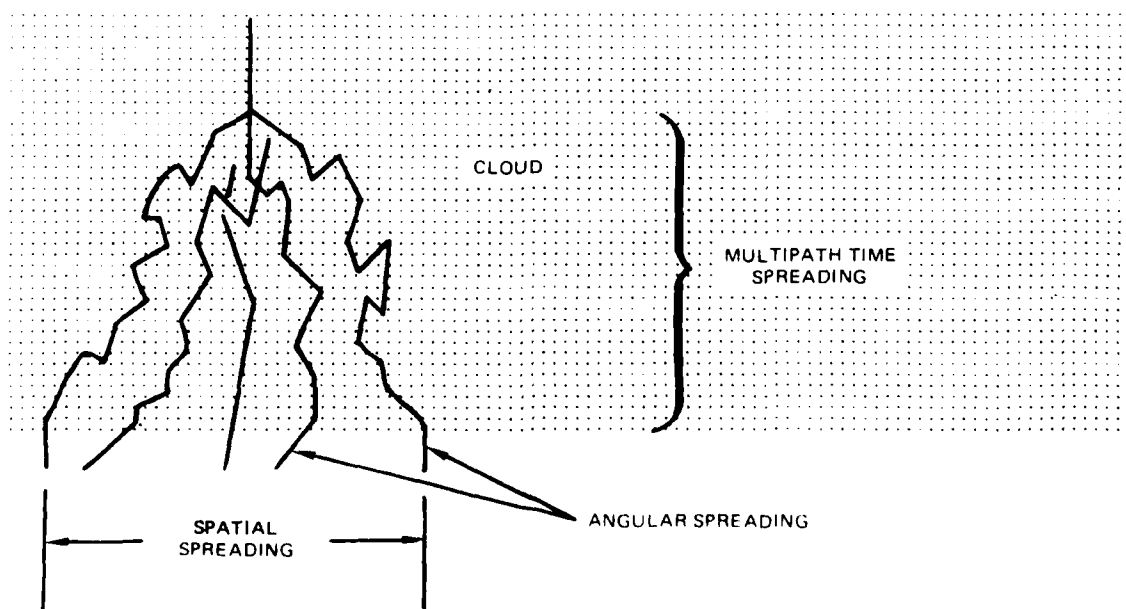


Figure 6. Parameters of light propagation in clouds.

### 2.5.2 Angular Spreading

For simulations involving clouds with  $\tau_d \geq 2$ , Bucher found the distribution of exit angles relative to the cloud's normal to be fairly uniform in brightness. That is, he observed that the exit angles for rays emerging from a given area on the bottom boundary tended to be concentrated within a  $45^\circ$  cone about the normal. However, when a projected area correction factor of  $1/\cos \phi_E$ ,  $\phi_E$  being the exit angle, was applied to the data, the resulting distribution did not contradict a hypothesis of uniform brightness in the bottom boundary when viewed from all angles.

With thin simulated clouds, Bucher observed a sharply peak distribution of exit angles centered around the straight-through axis. In addition, the peak was found to contain much more transmitted radiation than just the contribution of the direct extinction beam. He attributed this additional irradiance to a strong forward scattering behavior. In particular, he found, using the Mie series scattering function, that the peak was most pronounced within  $5^\circ$  of the normal and that the contribution was generated within 0.08T of the central point where the unscattered ray would exit. Figure 7 shows a plot of the fraction of total incident rays exiting the cloud generated during the simulation as a function of optical thickness in relation to the unscattered component. Bucher postulated that this multiple forward scatter component may be quite useful in some optical communication situations, e.g., over-the-horizon communications.

### 2.5.3 Spatial Spreading

Spatial spreading was measured by Bucher in terms of two criteria. Both of these criteria were based on the radius  $r$  defined previously as the distance from the exit point to the straight-through axis on the bottom boundary (see fig 5). Typically, the  $r$  distribution had long tails with some rays having a radius several times the average. Thus Bucher chose to characterize spatial spreading by the average radius  $\langle r \rangle$  and the exit radius  $r_c$  inside which half the transmitted rays exited the medium. Figure 8 shows  $\langle r \rangle/D_d$  as a function of  $\tau_d$  for the various scattering functions used. Figure 9 shows  $r_c/D_d$  as a function of  $\tau_d$ . The parameter  $D_d$  is given by the equation

$$D_d = D/(1-\langle \cos \theta \rangle)$$

where both  $D$  and  $\langle \cos \theta \rangle$  have been defined previously. Figure 10 depicts  $\langle \cos \theta \rangle$  as a function of the normalized Mie scattering parameter. For the scattering medium modeled,  $\pi D/\lambda$  ranged from 17.05 to 21.54, thereby giving a value of .81 for  $\langle \cos \theta \rangle$ . This implies  $\tau_d \approx 5.26 \tau$ . It is apparent from figures 7 and 8 that common behavior for all three scattering functions occur for  $\tau_d \geq 3$ . Furthermore, Bucher found that he could approximate these curves using the equations

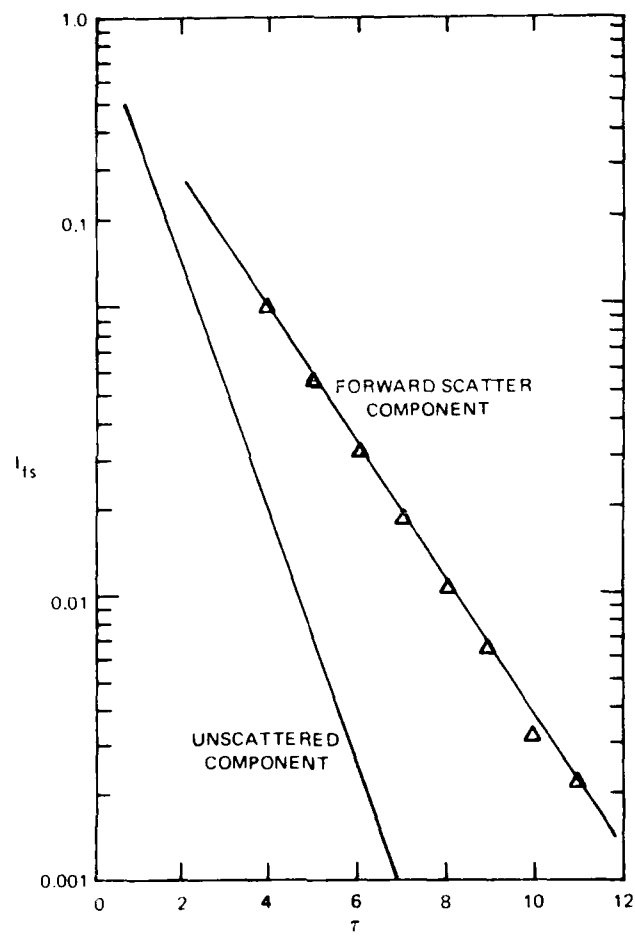


Figure 7. Intensity of the forward scatter and unscattered components. [12].

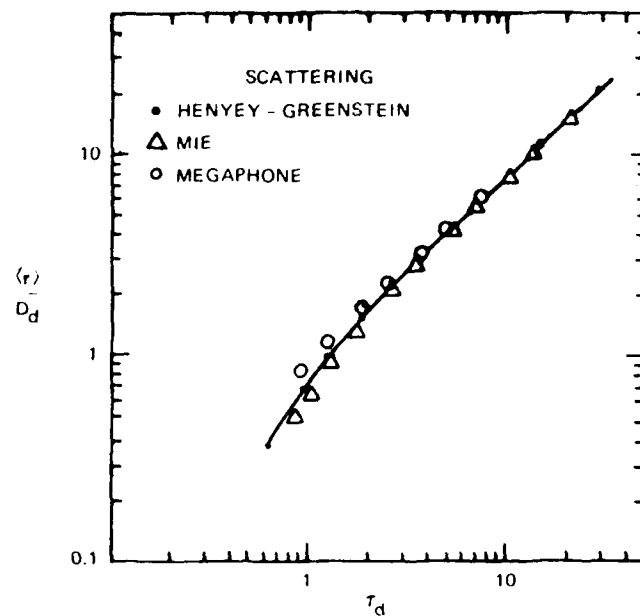


Figure 8.  $\langle r \rangle / D_d$  as a function of  $\tau_d$ . The 90% confidence limits on all data points are  $\pm 5\%$  or better. [12].

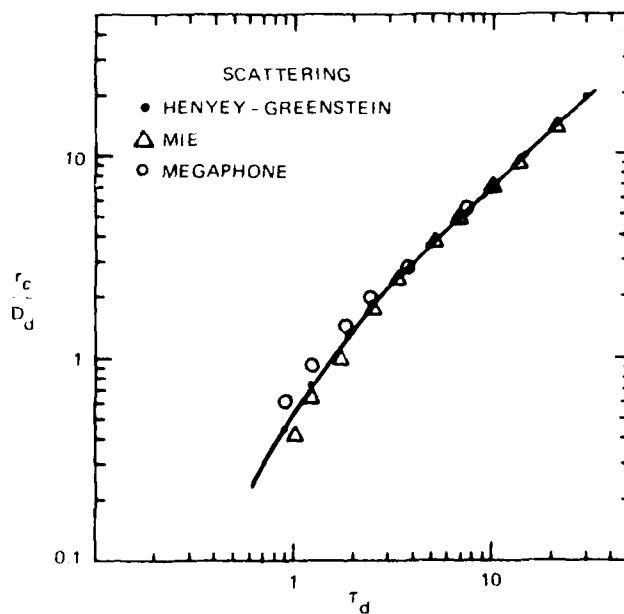


Figure 9.  $r_c / D_d$  as a function of  $\tau_d$ . The 90% confidence limits on all data points are  $\pm 5\%$  or better. [12].

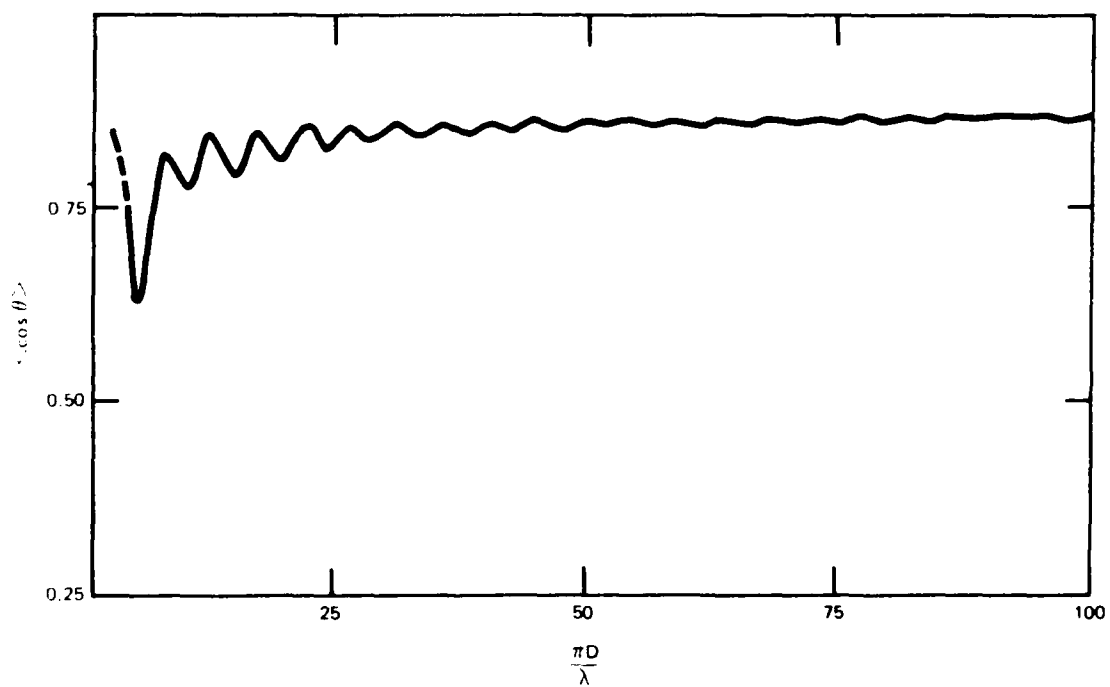


Figure 10.  $\langle \cos \theta \rangle$  as a function of the Mie scattering parameter  $\pi D/\lambda$ . [12].

$$\langle r \rangle = 0.92 \, \eta_d (\tau_d)^{0.92} \quad (33a)$$

$$r_c = 0.78 \, \eta_d (\tau_d)^{0.93}, \quad (33b)$$

respectively, for  $\tau_d > 3$ . Recalling the relationship between  $T$  and  $\eta_d$ , we see that the above expressions can be rewritten as

$$\langle r \rangle = 0.92 \, T (\tau_d)^{-0.08} \quad (34a)$$

$$r_c = 0.78 \, T (\tau_d)^{-0.07}, \quad (34b)$$

respectively. With this normalization, we see that the spatial spreading saturates and even decreases as a cloud of fixed thickness becomes more optically dense. This is reflected in figures 11 and 12 for  $\langle r \rangle$  and  $r_c$ , respectively.

#### 2.5.4 Multipath Time Spreading

In characterizing multipath time spreading, Bucher found it necessary to use three statistical measures: the mean pulse width  $\langle t \rangle$ , its standard deviation  $\sigma_t$ , and the width of the most intense central portion of the time distribution. This latter parameter, which is the multipath time spread  $L$ , is defined as the shortest range of multipath time values which encompass 63% of the total transmitted rays.

Figures 13-15 show  $\sigma_t$ ,  $\langle t \rangle$ , and  $L$ , respectively, as a function of the diffusion depth  $t_d$  for a variety of optical thicknesses ranging from 5 to 120. It is apparent that all three scattering functions give approximately the same measures for values of  $\tau_d > 2$ . The normalization factor  $t_d$  used in these figures is given by the equation

$$t_d = \eta_d / c$$

where  $c$  is the speed of light in air. Bucher then went on to show that the three statistical measures could be presented as

$$\langle t \rangle = 0.62 \, t_d (\tau_d)^{1.94} \quad (35a)$$

$$\sigma_t = 0.64 \, t_d (\tau_d)^{1.81} \quad (35b)$$

$$L = 0.74 \, t_d (\tau_d)^{1.83} \quad (35c)$$

for  $\tau_d > 3$ . It can be easily shown that the above expressions can be rewritten as

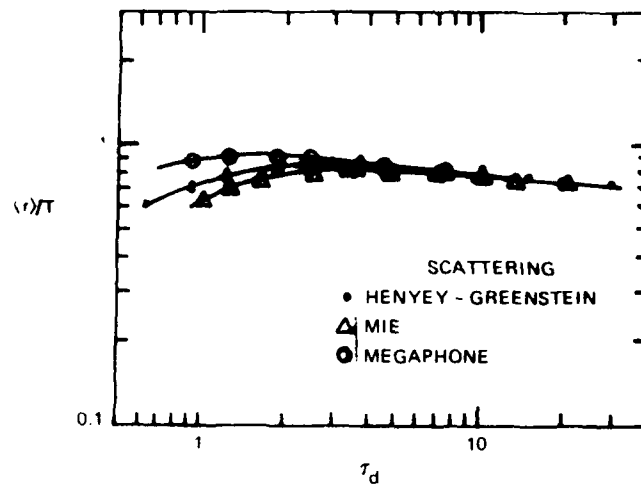


Figure 11. Plot of  $\langle r \rangle / T$  as a function of  $\tau_d$  showing the saturation in spatial spreading as a cloud of fixed physical thickness  $T$  becomes optically thicker. [12].

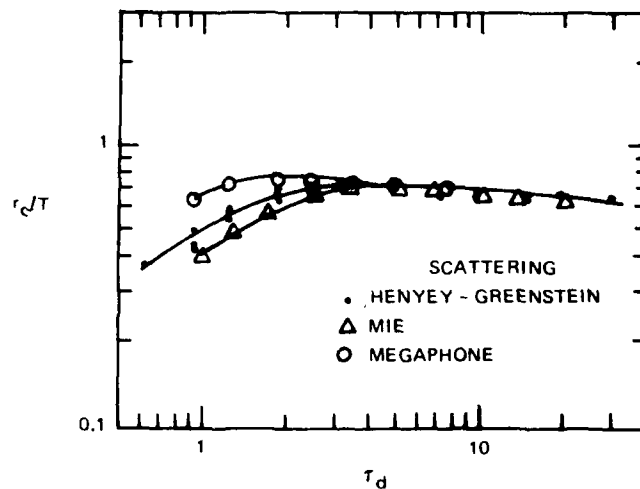


Figure 12. Plot of  $r_c / T$  as a function of  $\tau_d$  showing the saturation in spatial spreading as a cloud of fixed physical thickness  $T$  becomes optically thicker. [12].

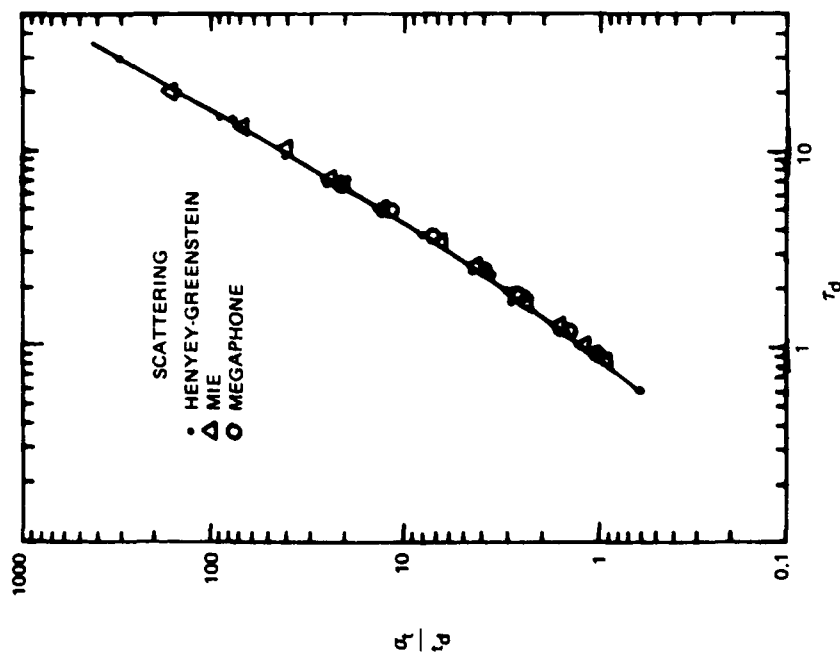


Figure 13.  $\sigma_t / D_d$  as a function of  $\tau_d$ . The 90% confidence limits on all data points are  $\pm 5\%$  or better. [12].

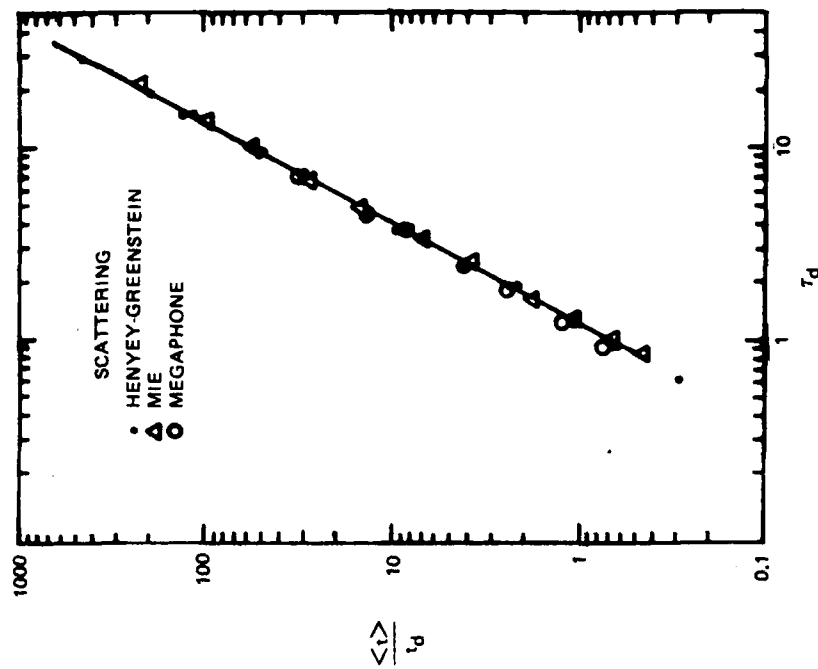


Figure 14.  $\langle \sigma_t \rangle / D_d$  as a function of  $\tau_d$ . The 90% confidence limits on all data points are  $\pm 2.5\%$  or better. [12].



$$\langle t \rangle = 0.62 T (\tau_d)^{0.94} \quad (36a)$$

$$\sigma_t = 0.64 T (\tau_d)^{0.81} \quad (36b)$$

$$L = 0.74 T (\tau_d)^{0.83} \quad (36c)$$

It is easily seen from the above that the time spread for sufficiently thick clouds grows in a way that is essentially independent of both the details of the scattering function and of the width-measuring criteria.

### 2.5.5 Total Transmission

It can be shown [22,23] that the fraction of incident rays transmitted through a "thick" cloud of nonabsorbing scatterers is given by

$$I_t = A / (\tau_d + B), \quad (37)$$

where A is a function of the incidence angle, and B is essentially a constant. For normally incident radiation, this asymptotic expression becomes

$$I_t = 1.69 / (\tau_d + 1.42). \quad (38)$$

Figure 16 shows a plot of simulation  $I_t$  and the  $I_t$  predicted from the above equation as a function of  $\tau_d$ . As one can see, there is very good agreement between the two formulations. Thus we have an analytical expression for  $I_t$  in terms of the weighted optical thickness.

## 3.0 EXPERIMENTAL TEST PLAN

### 3.1 Goals of the Program

The basic measurement proposed here is to determine the time history of a short laser pulse that has propagated through a path of fog particles characterized by drop-size distributions and spatial extent. The power loss, the pulse spreading and the pulse delay will be measured as a function of receiver FOV for various types of marine coastal fog. Direct beam extinction coefficients will also be measured and compared with that derived from Mie theory using the measured drop-size distributions and readings from a visiometer. The laser beam for the experiments will be supplied by a frequency doubled (.53  $\mu$ m) neodymium YAG laser with an automated digital data acquisition system. The fog particle size distributions will be measured using two Knollenberg drop-size spectrometers situated selectively along the propagation path. For fog events which occur during daylight hours, their time history and spatial extent will be determined from time-lapse photographs taken at two separated locations. During night hours other atmospheric sensors (discussed in a following subsection) will be utilized. The laser, variable FOV receiver, drop-size spectrometers and other meteorological sensors to be used in the measurements are described in detail in different sections which follow.

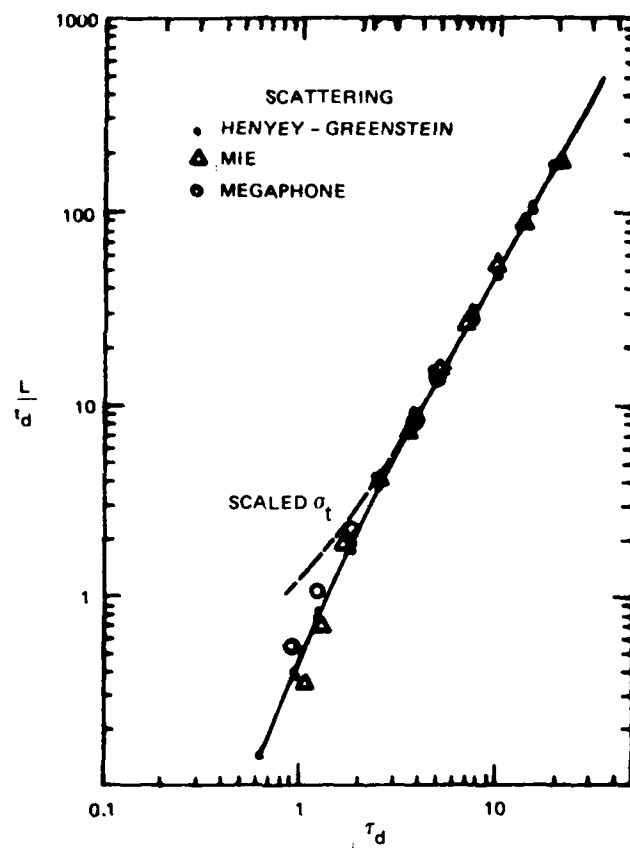


Figure 15.  $L/t_d$  as a function of  $\tau_d$ . The 90% confidence limits on all data points are  $\pm 7\%$  or better. [12].

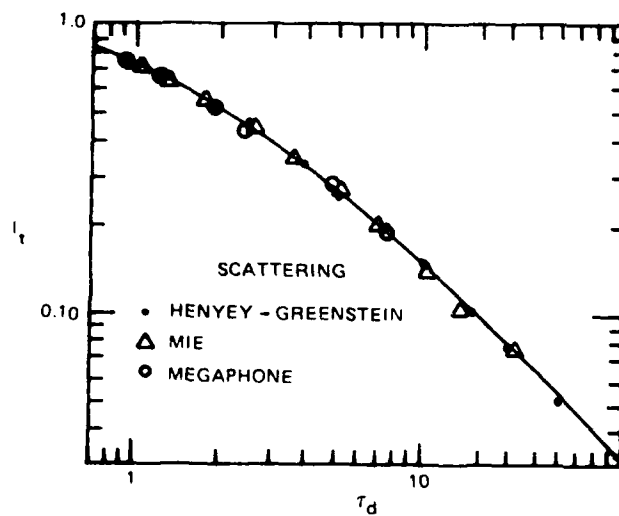


Figure 16. Total transmission as a function of  $\tau_d$ . The theoretical curve is from van de Hulst's work. The 90% confidence limits on all data points are  $\pm 5\%$  or better. [12].

### 3.2 Rationale for Selection of Site

Ideally, the measurements should be conducted from an aircraft to a receiver on the ground. However, the cost and equipment available presently prohibit this approach. An equally acceptable configuration would be through a vertical section of clouds down a mountain slope or between two mountain peaks where the clouds are typically of marine origin (as exists on the island of Hawaii). However, for the preliminary measurements a site located on Point Loma, San Diego, California, has been chosen. This site is a compromise based on economics and time. The selected propagation path is shown in the aerial photograph of Point Loma, figure 17. The two terminals of the propagation link are separated by 2.4 km and located at NELC's Battery Ashburn facility and the remote sensing facility, Building T323. The elevations above MSL are 377 feet and 105 feet, respectively.

The advantages of the Point Loma location are: (1) easily accessible and located on government property; (2) the propagation path is in proximity to the remote sensing facility for assessing the propagation medium; (3) considerable marine fog (visibility less than 1 mile) occurs along the coast during the fall and winter months (see figure 18); and (4) other conditions of reduced visibility (less than 5 miles) also frequently occur in the winter and summer months (see figures 19 and 20). The Fleet Weather Service located at nearby North Island Naval Air Station is also available for fog forecast such that personnel can be alerted and equipments made operational during periods of high probability for fog occurrence.

Generally, two types of fog prevail along the Point Loma coast, namely stratus-cloud and Santa Ana fog. The mechanisms producing each fog type appear to be distinctly different. Stratus-cloud related fog is a mid-calendar year phenomenon and is produced when the base of the stratus clouds descends to the ground, usually at night. Evidence indicates that a sequence of events initiated by radiation cooling at the cloud top causes the cloud base to descend slowly. The visibility in this type of fog seldom reduces below 1/4 mile, which is typical when marine aerosols are involved.

Fog related to wintertime Santa Ana conditions appears to have two formation mechanisms. However, both types of fog appear to be transported into the San Diego region by the movement of mesoscale troughs at different orientation. One type of Santa Ana related fog usually moves into San Diego as a diffuse or sharp fog bank. The other, and less common, Santa Ana fog moves as a low thin deck (about 30 to 50 m thick) northward from the coast of Baja California into the San Diego region. Although the fog formation mechanism and mesoscale circulation associated with Santa Ana conditions are not generally known, there appears to be relation between the wet bulb temperature of the continental air which moves out over the ocean and the sea surface temperature which results from ocean current up-welling along the coast. Because of the smaller-sized continental aerosols involved, this type of fog is much more dense than the stratus-cloud type and provides the best opportunity for observation of the pulse stretching effects. Also, since the Santa Ana fogs approach the propagation path from the west and south, various conditions exist which allow the laser source and receiver to be both or separately immersed in the fog.

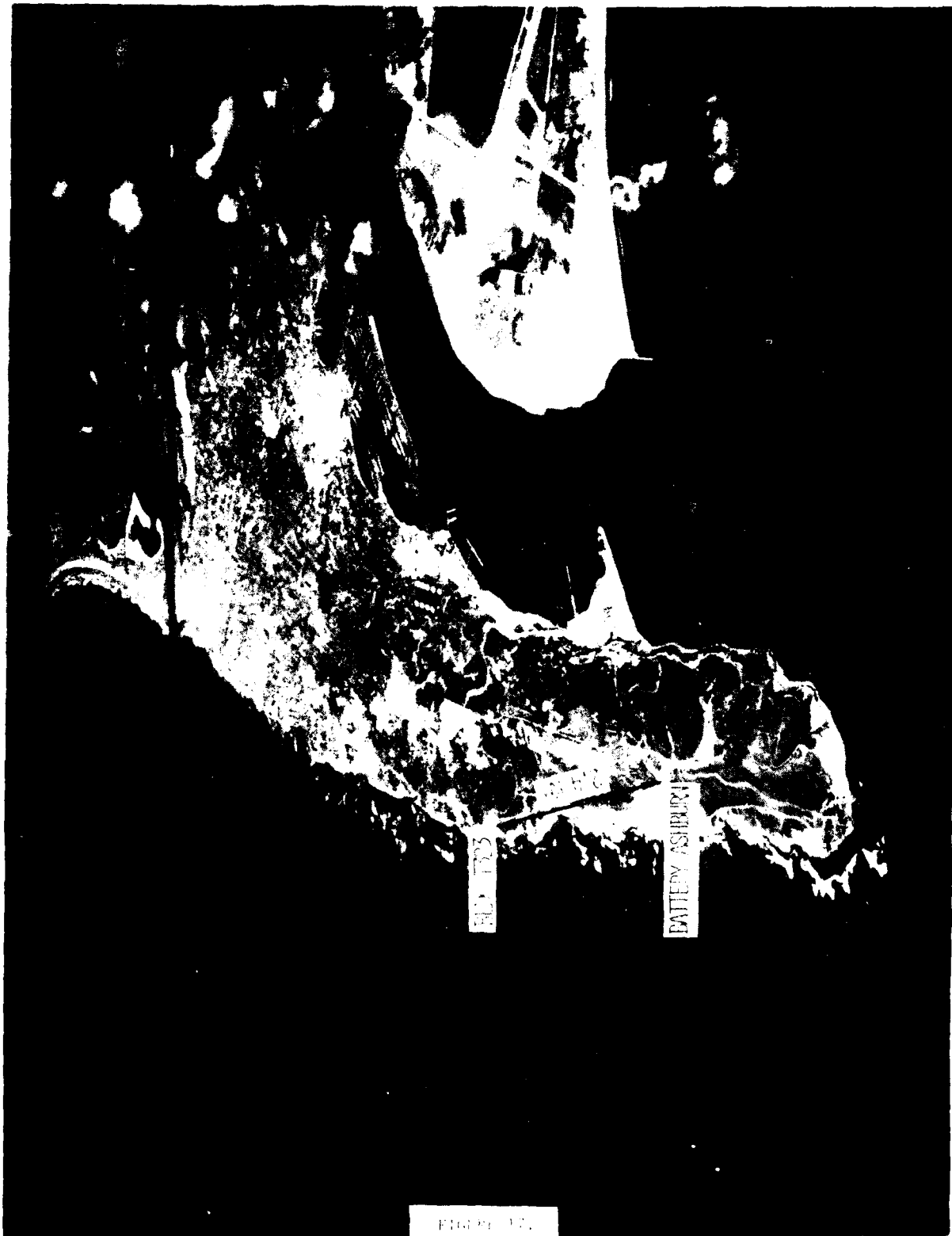
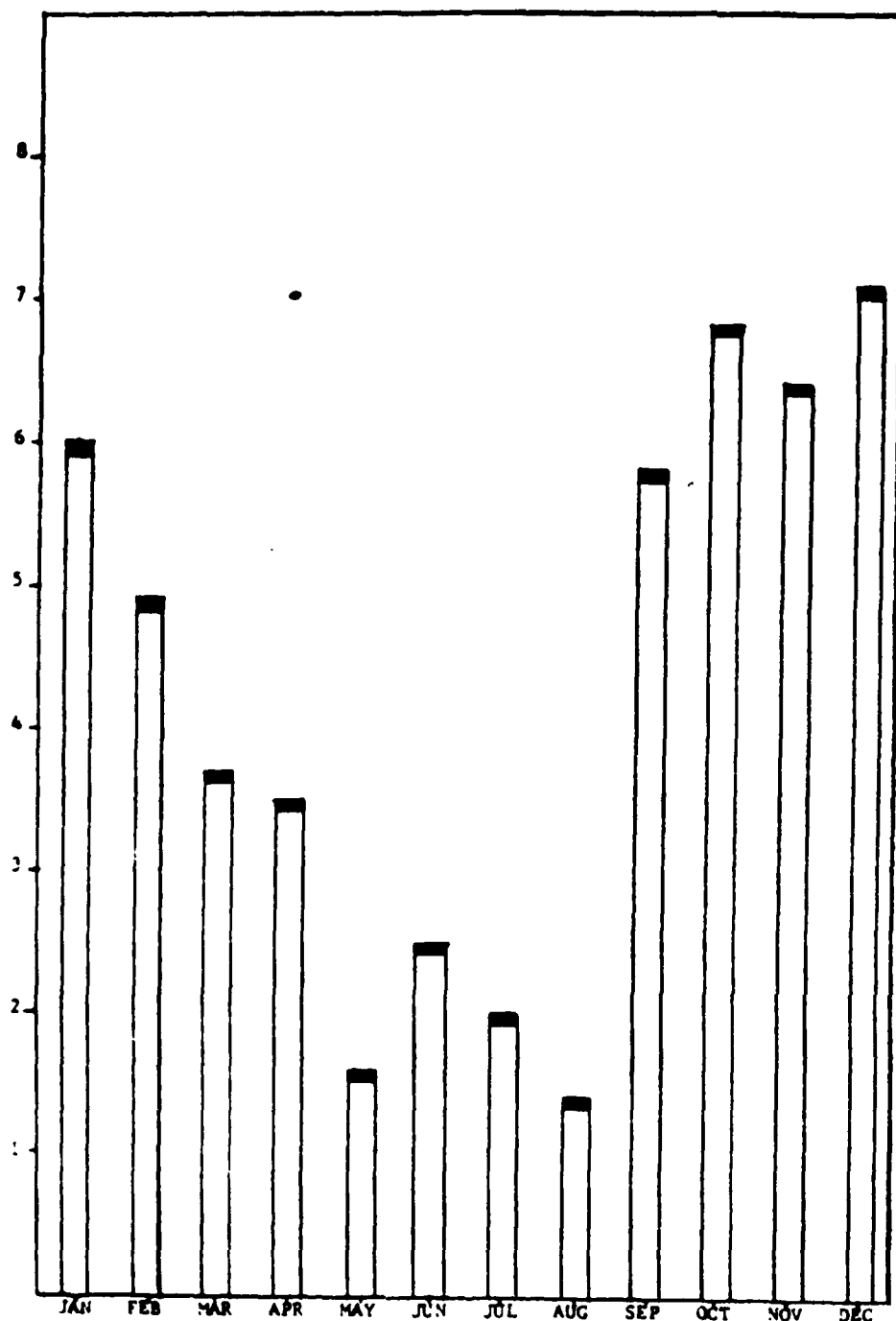


FIGURE 17.



Number of days of fog observed with visibility less than one mile.

1946 THRU JULY 1968

FIGURE 18.

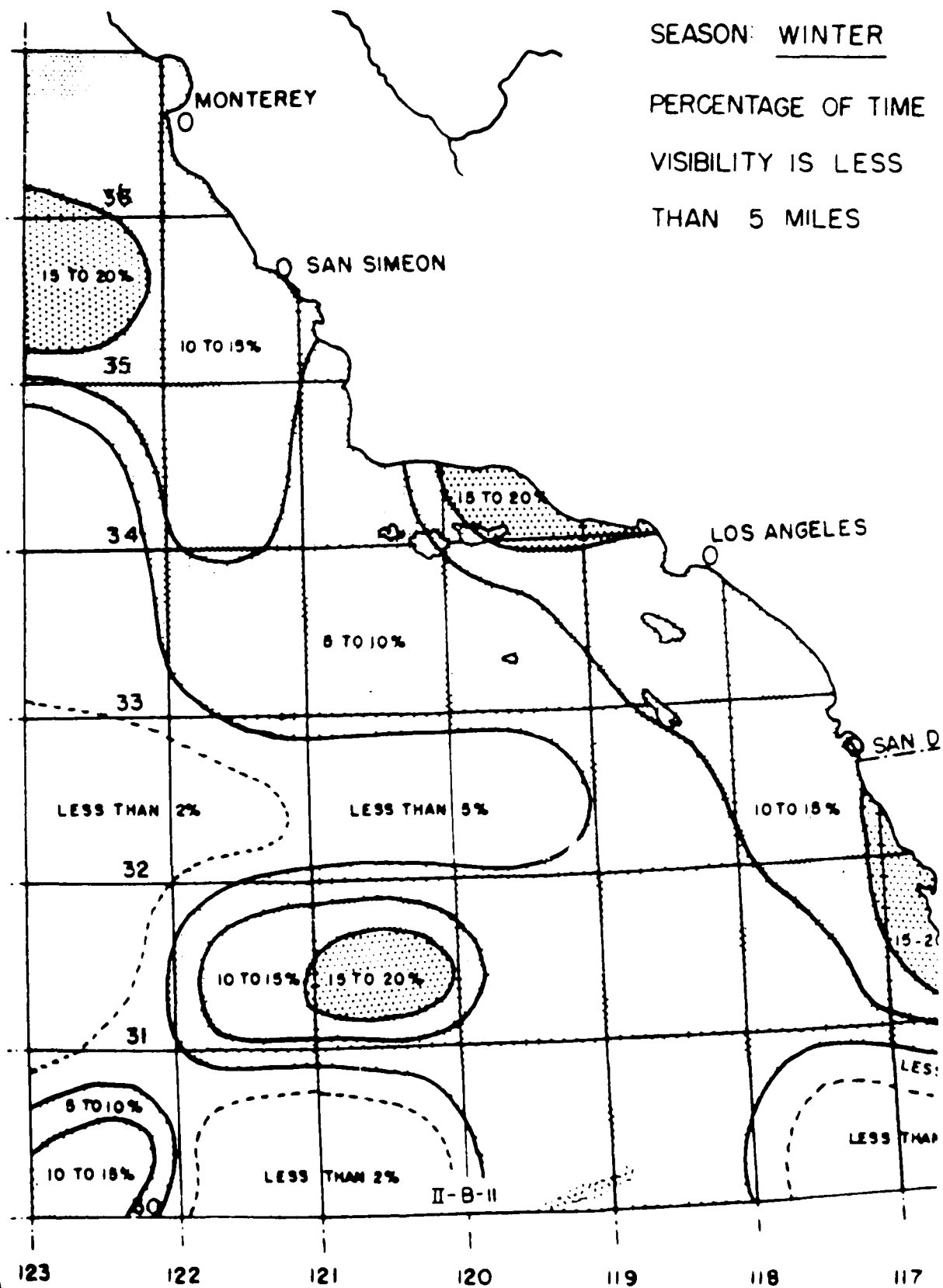


FIGURE 19.  
37

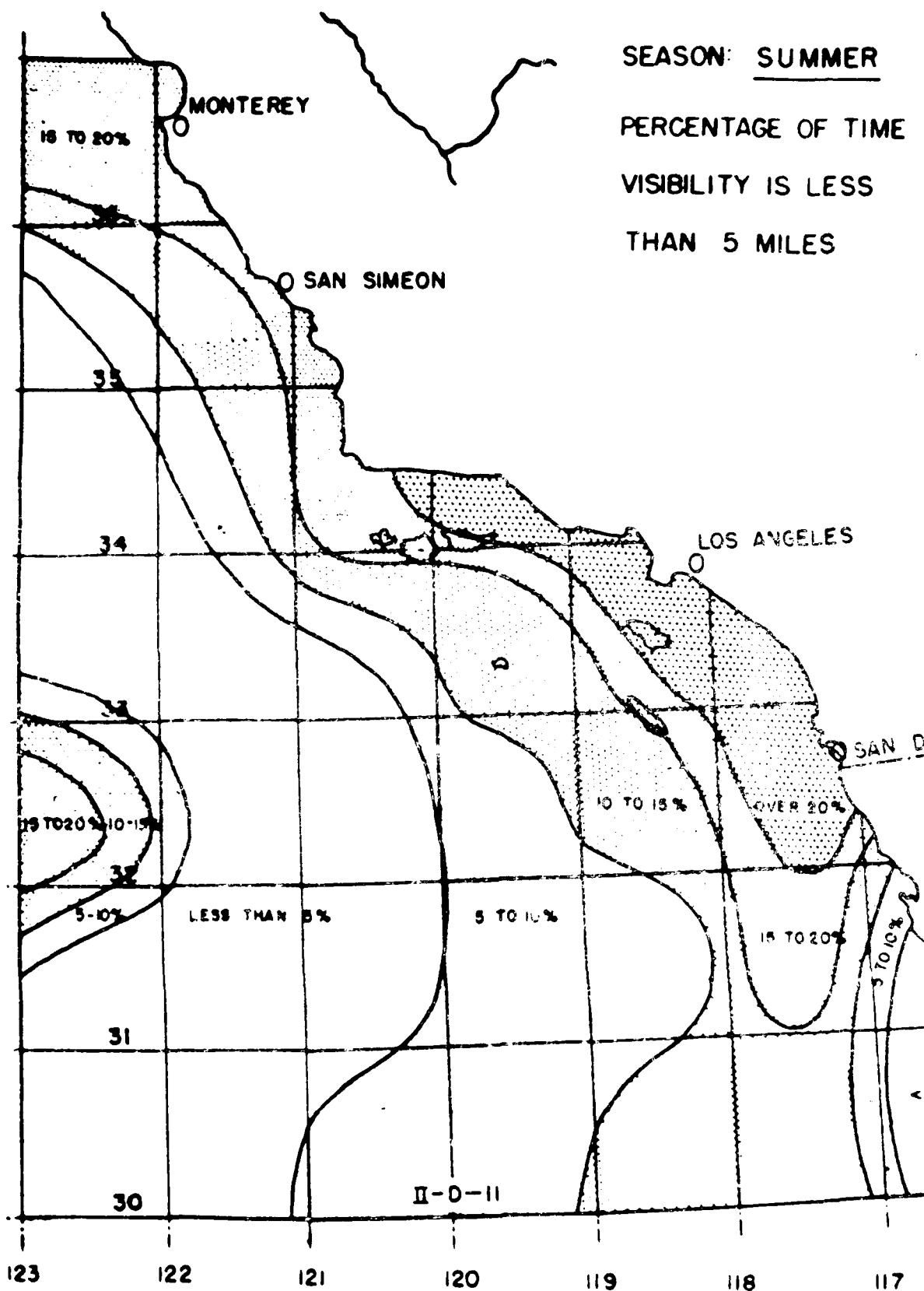


FIGURE 20  
38



A recognized disadvantage of utilizing the Santa Ana fogs for the propagation experiments is that they are contaminated by continental aerosols and may not be typical of clouds which occur over remote areas. Also, the vertical gradients in the aerosol distributions and temperature moisture profiles experienced in the low-level propagation path will not be the same as for elevated oceanic clouds. Needed is the ability to extrapolate the data acquired in the coastal fogs to the open ocean environments. Given the drop-size distributions and spatial variations, computer codes need to be developed to predict the multiple scattering propagation effects for various types of oceanic fogs and clouds. These computer programs involve complicated Monte Carlo techniques which are expensive to develop and process by digital computer and are beyond the scope of the measurement program proposed here. However, the multiple scattering codes require as inputs the single particle scattering Mie coefficients. Computer codes for these Mie coefficients and their integration with drop-size distributions to obtain extinction coefficients presently exist at NELC. These programs were developed by NELC and MEGATEK Corp. in support of the NELC OCCULT (Optical Covert Communications Using Laser Transceivers) system. As mentioned earlier, the singly scattered direct beam extinction coefficients will be measured using a narrow FOV receiver. These measured values will then be compared to those calculated with the computer codes using measured drop-size distributions.

### 3.3 Proposed Measurements

As discussed in section 3.1, the goals of this experimental test plan are:

- a. The measurement of the time history of the radiant power of a light pulse after propagating through various clouds or marine aerosols; and
- b. The determination and the quantification of the various loss mechanisms inherent to the aerosols.

The measurements and the presentation of the data will be in a form compatible with the needs of the optical communication systems engineer. That is, the subsequent results and conclusions derived from this program will enable the optical system designer to predict communication link performance and thereby allow system design optimization. Let us now discuss the proposed measurements in more detail.

Consider a laser source emitting  $P_t$  watts with beam divergence . The power received  $P_R$  at a distance  $R$  with a receiver possessing an antenna of area  $A$  is approximately

$$P_R = P_t \left[ \frac{A}{(2R)^2} \right] \quad (39)$$

neglecting atmospheric losses. If we now intersperse a turbid medium, absorption losses are negligible compared to the losses induced by scattering, i.e.,  $\omega_0 \approx 1$ . The power then received at the receiver, assuming very thin clouds, is given by

$$P_R = P_t \left[ \frac{A}{(\theta R)^2} \right] e^{-k_{\text{scat}} R} \quad (40)$$

where  $k_{\text{scat}}$  is the single scattering coefficient previously described in section 2.2.1. With nominal values of  $k_{\text{scat}}$  occurring in clouds, the practical possibility of attaining optical communication through clouds using the direct beam would be ruled out. For example, fair weather cumulus clouds possess a scattering coefficient on the order of  $5 \times 10^{-2} \text{ m}^{-1}$ . If the cloud has a physical thickness of 1 km, the path loss due to single particle scattering would be 100 dB. It is implied in the direct beam formalism that any photon scattered is completely lost and will not be collected by the receiver. This large value of path loss, 100 dB, in addition to other incurred losses would severely inhibit the potential of communication through clouds. However, since the forward scattering process does not absorb photons, but merely redistributes them both temporally and spatially, collected scattered irradiance could possibly provide a means to enhance open channel communications availability.

The equation for received scattered power given above (Eq. 40) assumes that the scattering by atmospheric clouds is isotropic in nature, i.e., the scalar phase function  $p(\gamma, \gamma')$  is defined to be unity. However, this is not the case in real life. Calculations using Mie theory show that the scattering by atmospheric aerosols is not isotropic, but rather highly biased in the forward direction. Figure 21 illustrated a large scattering probability for angles less than 2 degrees, and then shows an order of magnitude reduction in probability to a value which remains constant for about 30 degrees. Beyond this angle, the scattering probability decreases by one or two orders of magnitude.

Figure 22 is a typical schematic representation of the laser source as it might be viewed by the receiver after being scattered by cloud aerosols. The central core (shown here as a dot) is the unscattered beam, which possesses microradian-type angular spread. Surrounding this is an aurora of width  $\theta_1$  (on the order of a few degrees) which consists of photons which have been scattered only a few times. Around this disc is an aurora of decreased brightness (although for large optical thicknesses, it contains most of the energy), with width  $\theta_2$  on the order of tens of degrees. Thus, increasing the field-of-view (FOV) of the optical receiver will, in general, increase the number of signal photons collected. One goal of these experiments is to measure the signal increase with FOV.

The temporal behavior of the received signal with increasing FOV will also provide needed information. The direct, unscattered beam maintains the same pulse shape as the initial pulse independent of optical thickness. As the FOV of the receiver is increased, the scattered photons that are captured by the receiver may increase the signal peak power, but will probably also lead to pulse stretching, and to the delay of the peak of the pulse. Thus, while pulse energy will increase, the peak power may remain the same, or increase slightly. The pulse can be stretched to values as

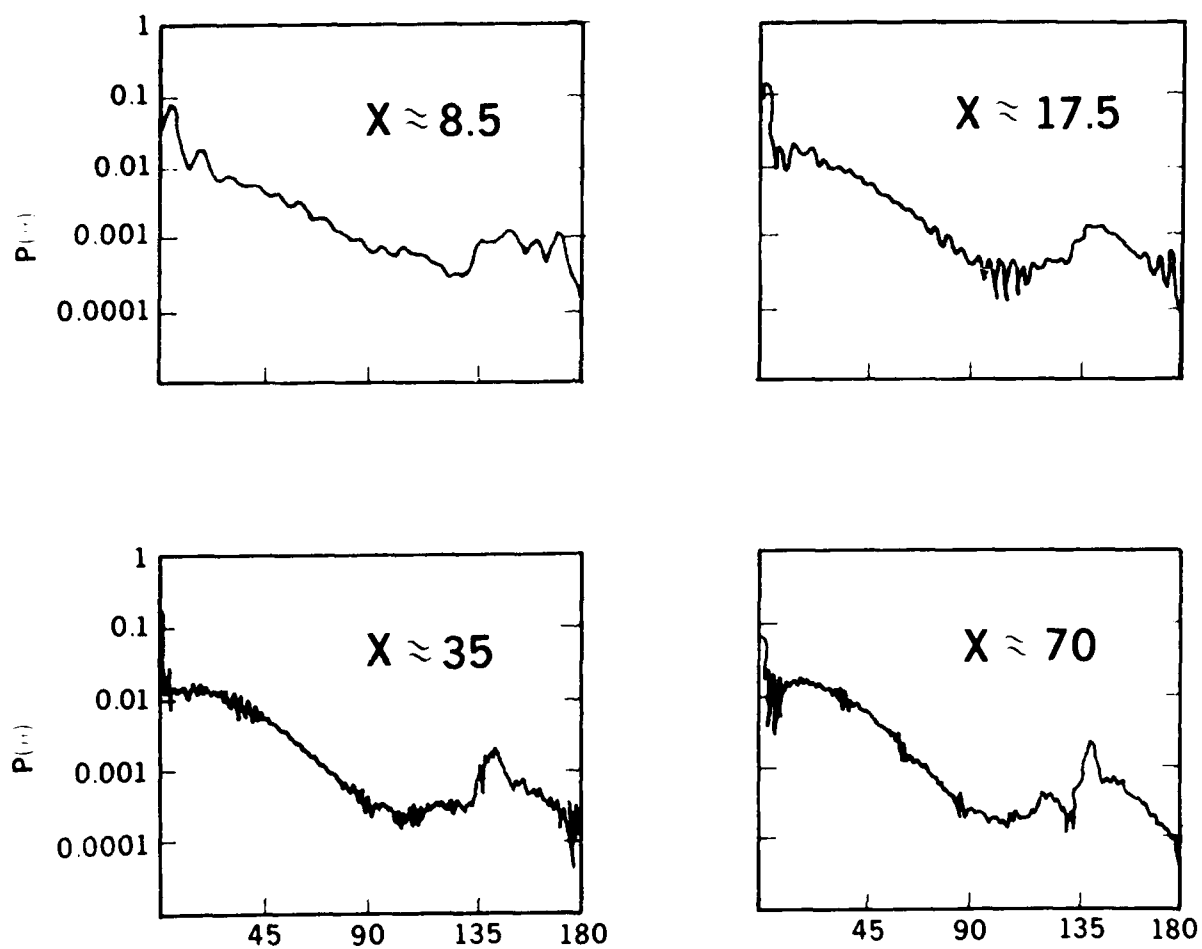


FIGURE 21. Mie scattering functions for various values of the Mie parameter  $x = \pi D / \lambda$ . [24]

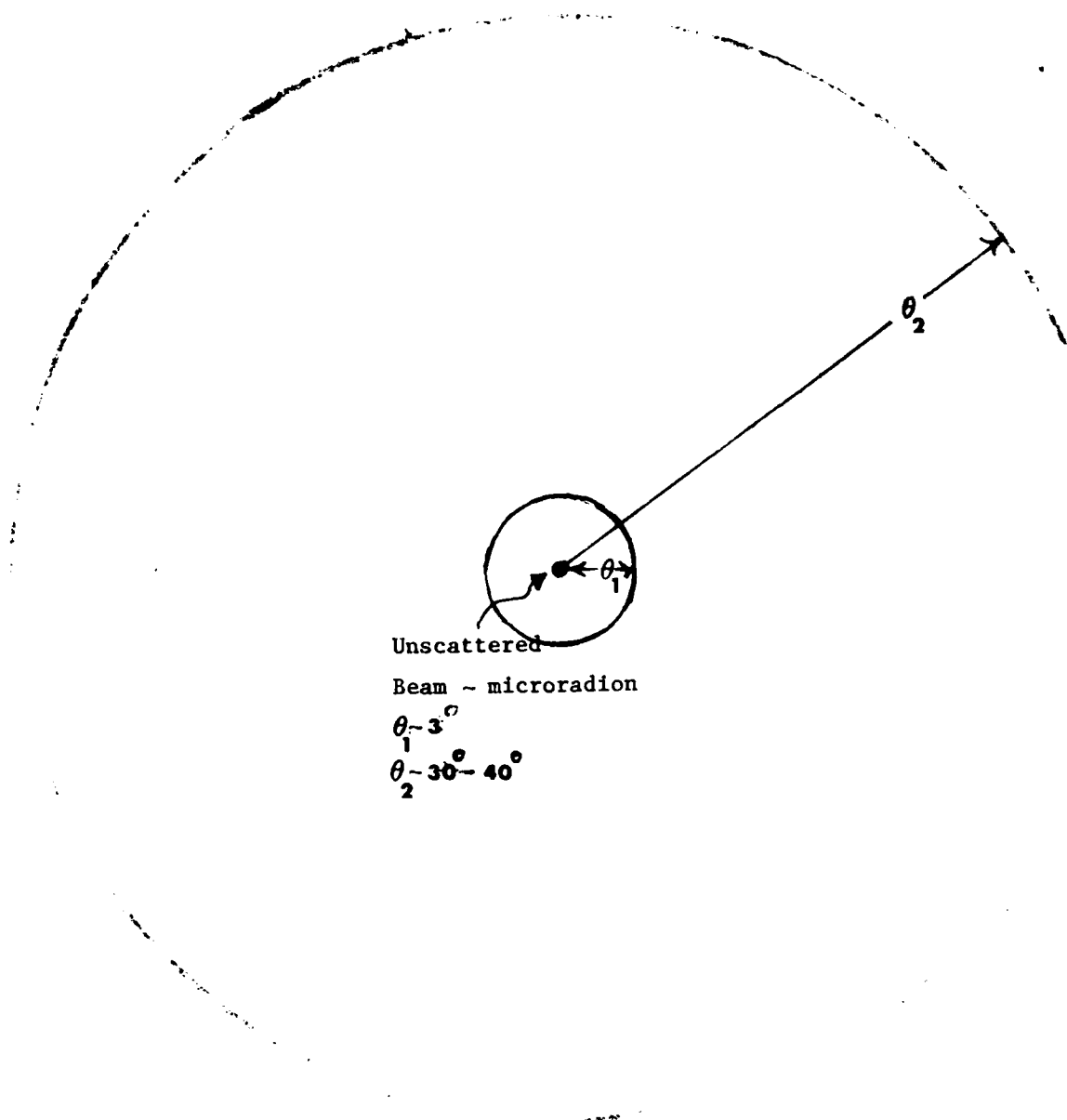


Fig.22: Schematic Representation of Laser Angular Brightness Distribution  
After Traversing a Cloud

(NOT TO SCALE)

large as tens of microseconds [24]. This will limit the data rate to tenths of megabits per second. More important, however, is the fact that the received peak power is reduced. This factor is very important to low bit rate communications since most conventional detection schemes respond to peak power inputs. In addition, the pulse stretching effect will impose longer integration times in photon counting systems. For example, if the received pulse width increases from 20 ns to 20  $\mu$ s, the photon counting interval must be increased by  $10^3$  in order to collect all the signal photons, and therefore increase the background noise count also by  $10^3$ . This "pulse stretching" loss is in addition to change in background noise resulting from increasing the field-of-view.

The transmitter components of the propagation link are shown in figure 23. The laser is a General Photonic Nd:YAG laser emitting 1 MW 20 nsec pulses at 1.06  $\mu$  with pulse rates to 10 pps. A frequency doubling crystal converts about 20 percent of this fundamental to first harmonic at .53 microns. The laser is triggered by a pulse generator, which will send out a synch pulse via a UHF transmitter to the receiver.

The components of the receiver are shown in figures 24 and 25. The .53  $\mu$  radiation is collected by a variable FOV telescope and detected by a calibrated photomultiplier tube. The output signal is digitized by a Biomation 8100 digitizer and then recorded on a tape deck and simultaneously displayed in real time on a scope. The sync signal from the transmitter is detected and used to arm the digitizer in preparation for the incoming pulse. The equipment for measuring the direct, nonscattered pulse is shown in figure 25. The .53  $\mu$  radiation is collected by an 8-inch Cassegrain telescope. The telescope has a very narrow FOV, and is bore-sighted with the transmitter to detect only the unscattered beam. The energy is again detected by a calibrated photomultiplier. A scope will monitor in real time the time history of the radiation. As no pulse distortion is expected of this direct beam, only the peak power has to be recorded. A circuit to sense and hold the peak voltage of the pulse will then record the value of peak power of every transmitted pulse. This will then allow determination of optical thickness of the path.

The most important measurement in this experiment is the time history of the pulse at the receiver as a function of FOV for various optical depths of fog conditions. This will yield the delay of pulse arrival time, the amount and extent of pulse stretching, and the calibrated photomultiplier tube will give the flux density at the receiver, from which the path loss will be calculated ( $P_{rec}/P_{trans}$ ).

From the measurement of the direct, nonscattered pulse power, an average value of single particle scattering,  $\beta$ , will be calculated. This value will be compared with that derived from the particle spectral density obtained from the Knollenberg counter and the Mie theory, and the value that is recorded from the visiometer.

TRANSMITTER

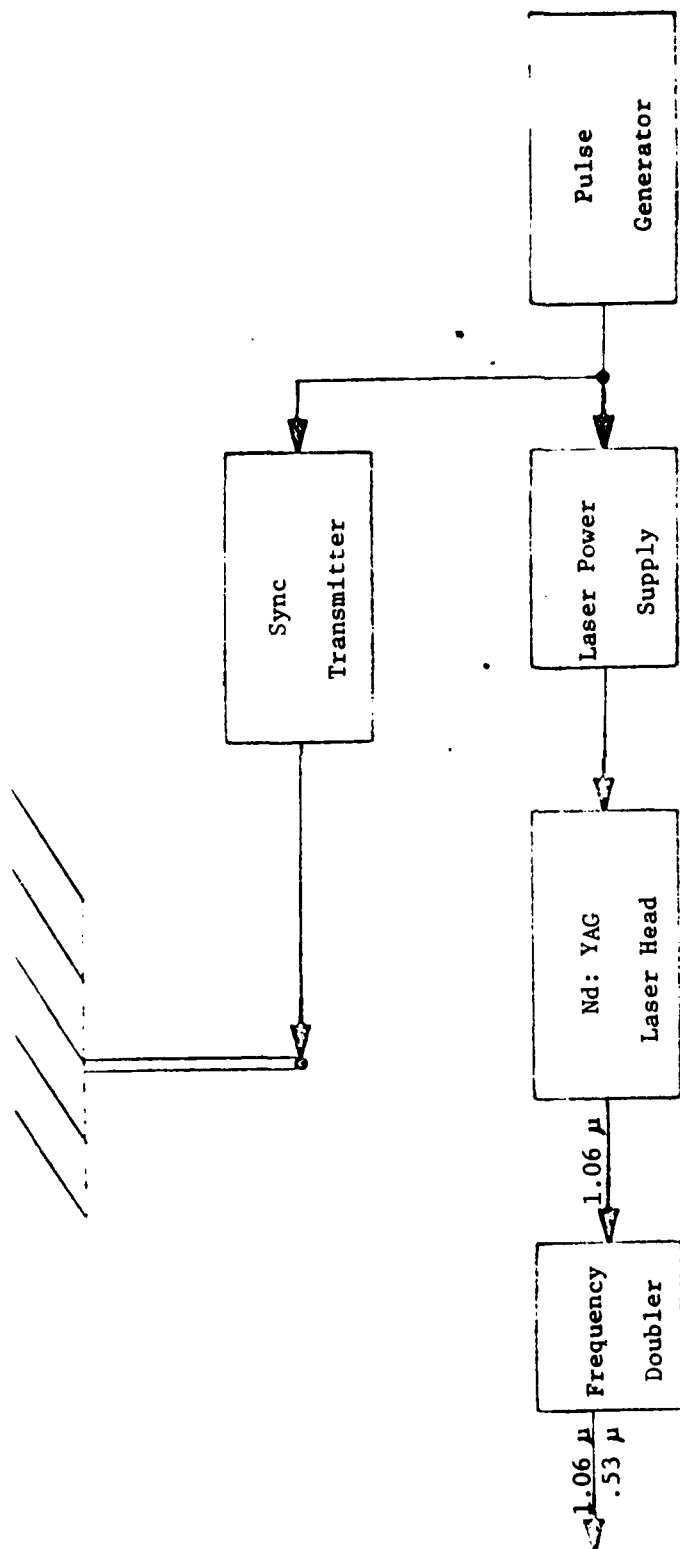


FIGURE 23

# RECEIVER FOR RECORDING TIME HISTORY OF PULSE

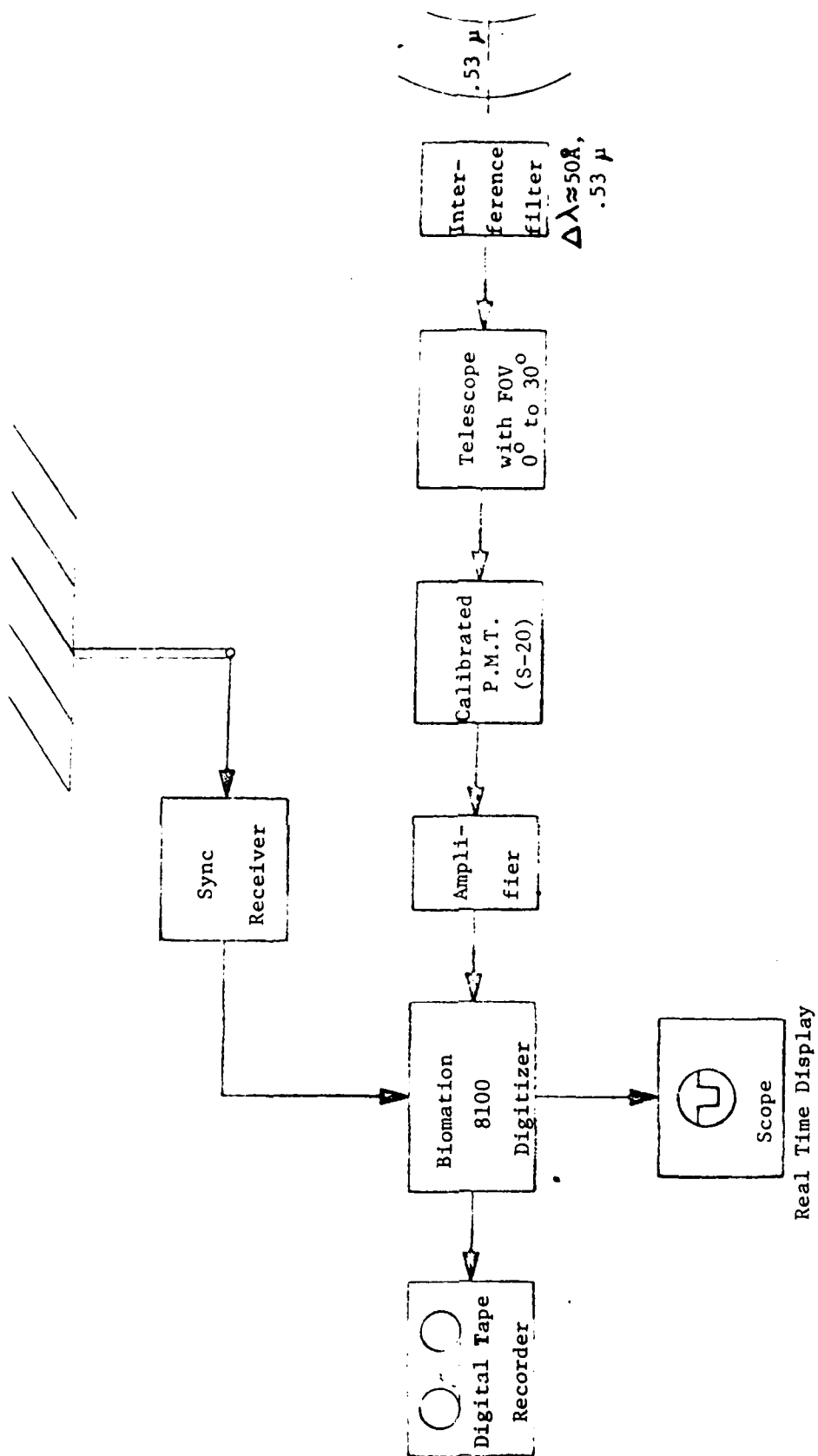


FIGURE 24

RECEIVER FOR MEASURING THE DIRECT, NON-SCATTERED PULSE

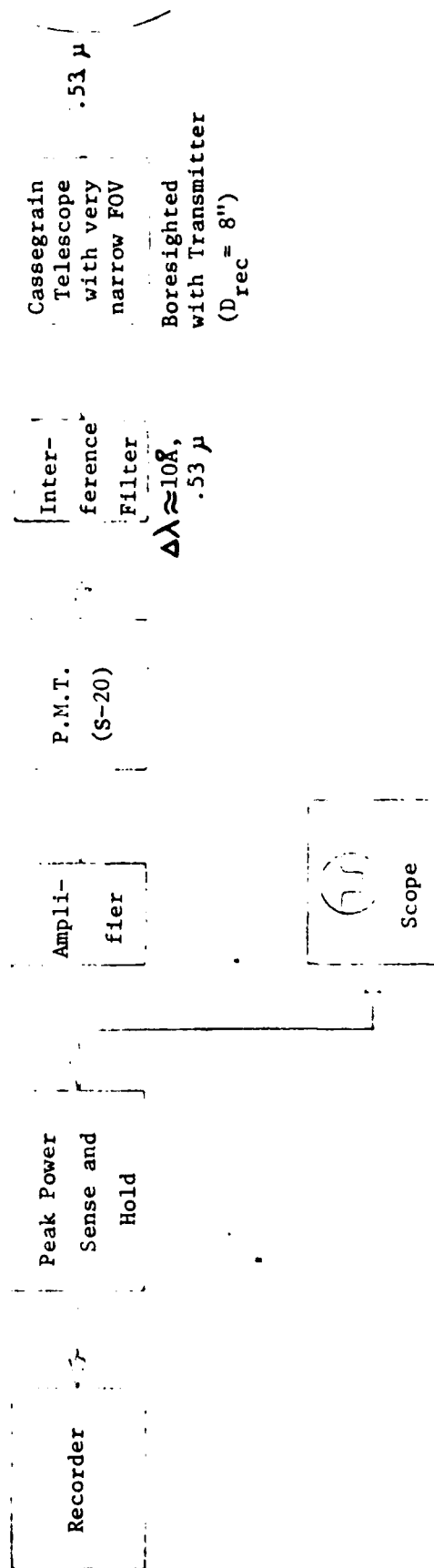


FIGURE 25



Figure 26 is a schematic set of curves, normalized to clear air spreading, of the data that is expected from this experiment. They are not to be taken too literally, but they should show general trends and shapes that might be expected. For small values of  $\tau$ , say  $\tau=1$ , the direct beam should dominate, and the path loss should be independent of FOV. Consider the path loss for  $\tau=5$ . For small FOV, the path loss is  $e^{-5}$ , or 22 dB. Increasing the FOV will increase the amount of energy that arrives from the forward scattered component,  $0 < \text{FOV} < \theta_1$ , and will probably saturate at  $\text{FOV} = \theta_1$ . Increasing the FOV further will probably not decrease the path loss, since for small values of  $\tau$  the first aurora has a substantially larger value of source brightness than the outer aurora. As  $\tau$  increases further, say  $\tau = 10$ , the brightness of the first aurora decreases, and the multiple scattering outer one increases. There should be an increase of signal for values of FOV greater than  $\theta_1$ . Saturation of signal should occur at FOV angles in the vicinity of  $\theta_2$ . For still further increases of  $\tau$ , say  $\tau = 20$ , the position of  $\theta_1$  is smeared out completely. Increase of signal should be observed smoothly from 0 degrees FOV to value larger than  $\text{FOV} = 30^\circ$ . The main goal of this experiment is the measurement of the exact shape of the curves in figure 26 and determination of propagation regimes.

As discussed above, the received signal is also expected to increase in pulse width with increase of FOV. For  $0 < \text{FOV} < \theta_1$ , the increase is expected to be small, as the scattering angles are small. But for  $\theta_1 < \text{FOV} < \theta_2$ , the pulse is expected to stretch by orders of magnitude. To remove a potential ambiguity in path loss of figure 26, we have defined the path loss in terms of the peak power as well as pulse energy. It will also be very informative to plot this curve from the data, with the vertical axes as the "Energy Path Loss" (integrating the received power over the pulse width to obtain received energy). As indicated in figure 26, while increasing the field of view can substantially increase received signal energy, in pulsed propagation the increase of field of view "may" only increase the pulse width and not the peak power, thereby yielding substantially different curves for the two cases. The determination of both these curves will be important to the system designer of an optical communications system operating through adverse weather.

### 3.4 Description of Atmospheric Sensors

Various atmospheric remote sensors currently are in use at or near NELC's Bldg. T323 and are available for assessing the propagation path for the proposed measurements. They include:

a. FM-CW Radars: Receives backscatter energy ( $\sim 3$  GHz) from refractive turbulent regions in the lower atmosphere. The humidity fluctuations account for essentially all of the backscatter. One radar is a fixed-position vertically pointing unit located at Bldg. T323 and the other radar is a mobile scanning unit. These systems provide a means of measuring the vertical extent of the fog layer.

b. Acoustic Echosounder: A vertically pointing system (2 kHz) receiving backscatter energy from regions of temperature fluctuations in the lower atmosphere. Using a transmitter and two receivers, the system is capable of measuring horizontal wind components in a near real-time mode to an altitude of 500 meters.

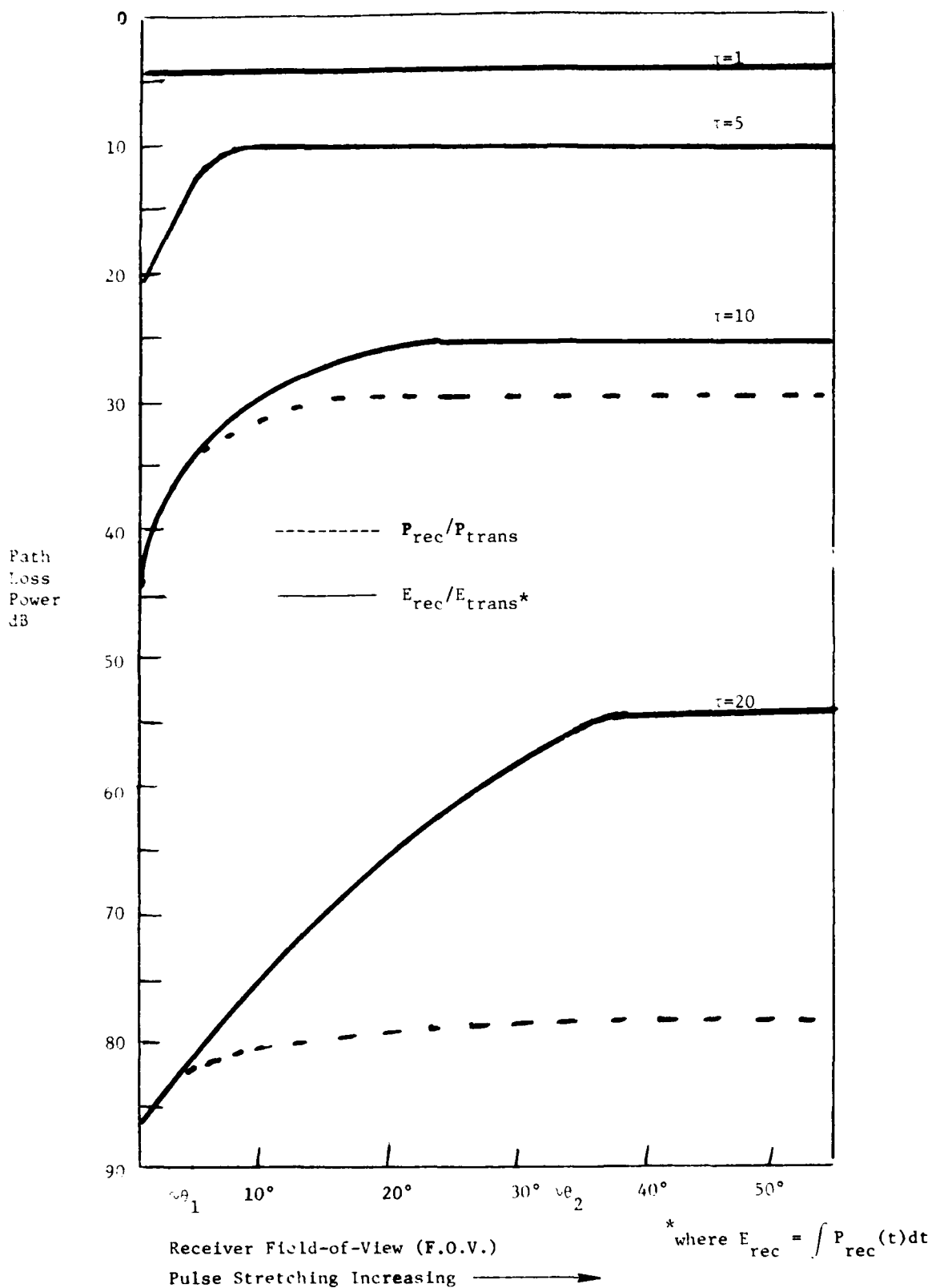


Figure 26: Path loss versus field-of-view for various optical thicknesses

c. Ceilometer (AN/GMQ 13C): A standard aircraft runway beam system (visible light, 400 ft. base leg) to measure the height of cloud bases.

d. Transmissometer (AN/GMQ 10C): A standard aircraft runway system for visibility measurements using a visible beam of light over a horizontal 500 ft. base leg.

e. Visiometer (MRI Model 1580A): A short-path (~ 2 feet) forward-scatter instrument to measure visibility out to about 10 km (with relative humidities up to 100%).

f. Integrating Nephelometer (MRI Model 1550): An instrument for measuring visibility out to about 50 km (with relative humidities less than 70%) by measurement of light scattered through a sample of aerosol laden air.

g. Radiosonde Sets: One set permits the measurement of winds, temperature and relative humidity from the surface to above the 100 mb level. The other set measures only temperature and relative humidity in the same altitude range.

h. Standard Surface Measurements: Continuous records are made of the surface temperature, wet-bulb wind and pressure.

i. Knollenberg Drop-Size Spectrometer: A system to continuously measure and record the drop-size distribution of aerosols either on the ground or airborne.

The location of each of these sensors in relation to Bldg. T323 is shown in figure 27. The instrument of most importance to these measurements is the Knollenberg drop-size spectrometer. This instrument determines aerosol-size distributions based on theoretical predictions of the scattering of light from a helium-neon laser (6328 Å) by spherical water particles. The system outputs are recorded digitally on magnetic tape and are computer processed to give the particle number density (particles/cm<sup>3</sup>/µm dia.). Table I shows a sample computer print-out of a distribution obtained during a dense Santa Ana fog which occurred on the morning of 25 June 1976.

### 3.5 Proposed Schedule

Item	Dates	
	Start	Complete
1. Initiate variable FOV construction	1 Oct 1976	30 Nov 1976
2. Install neodymium YAG laser at Battery Ashburn	1 Oct 1976	15 Nov 1976
3. Install data acquisition system at Bldg. T323	15 Oct 1976	30 Nov 1976
4. Initiate data acquisition period	1 Dec 1976	30 Apr 1977
5. Data analyses and final report	1 May 1977	30 Sep 1977

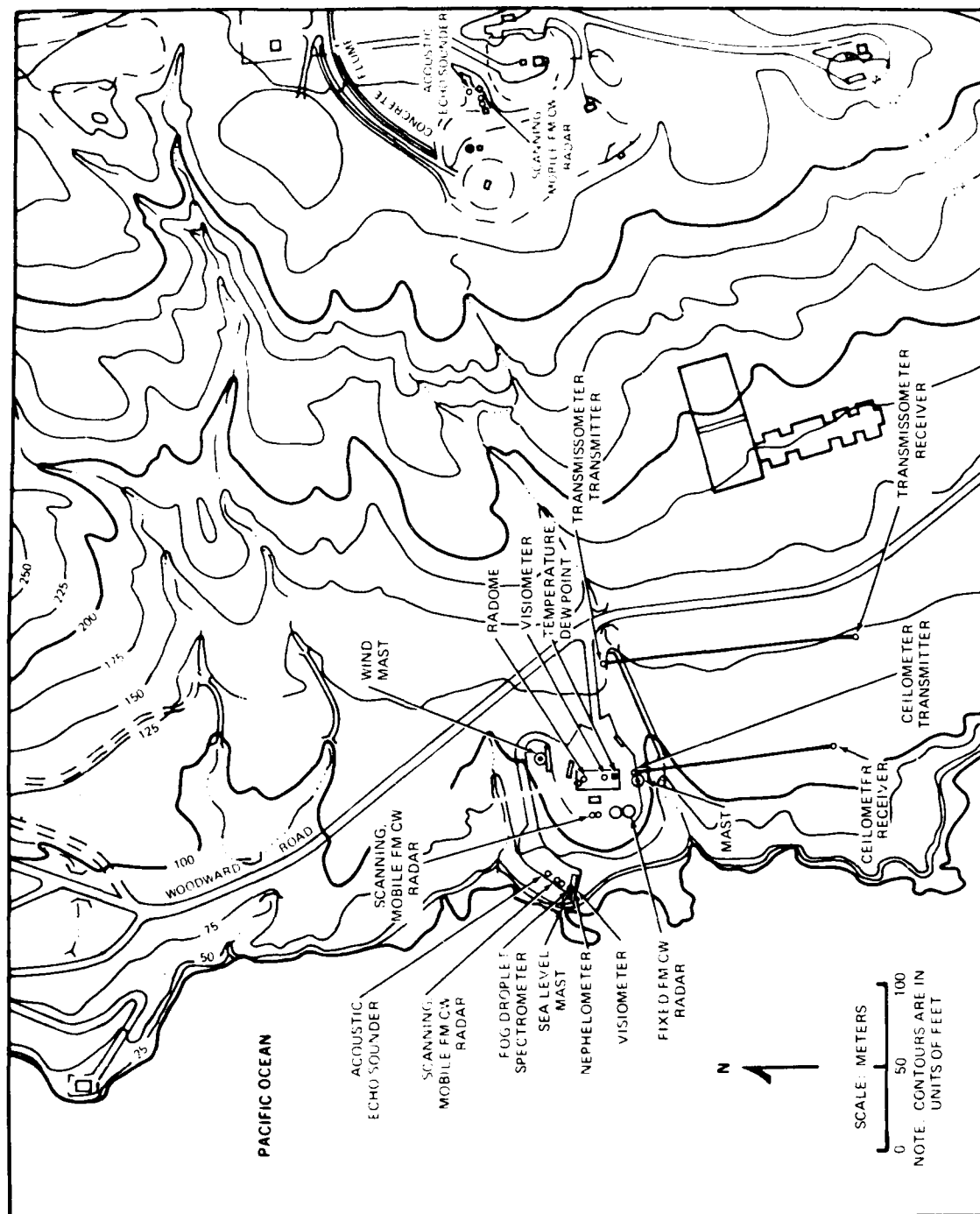


FIGURE 27.

1040: JUNE25, 1976 1453Z VEC.74-C.112MI 4 MIN SUM 60 SPEC/RANGE

CHL	DIA	COUNTS	DENSITY
1	.6	12799.C	.3969692+CC2
2	.9	19436.C	.6026667+CC2
3	1.2	20190.C	.6257364+CC2
4	1.5	20222.C	.6270389+CC2
5	1.8	19546.C	.6060775+CC2
6	2.1	18975.C	.5883721+CC2
7	2.4	19461.C	.4906579+CC2
8	2.8	16147.C	.5006822+CC2
9	3.2	15668.C	.4164252+CC2
10	3.6	14346.C	.3912890+CC2
11	3.9	16622.C	.3865581+CC2
12	4.3	16270.C	.3793721+CC2
13	4.7	16281.C	.3365581+CC2
14	5.2	15926.C	.3292196+CC2
15	5.6	13785.C	.2566465+CC2
16	6.8	16011.C	.1752230+CC2
17	7.6	10924.C	.1270233+CC2
18	8.4	6991.C	.9671008+CC1
19	9.1	4938.C	.6562126+CC1
20	9.9	3669.C	.4550698+CC1
21	10.5	2699.C	.3573422+CC1
22	11.5	3860.C	.3590698+CC1
23	12.5	3349.C	.3114419+CC1
24	13.5	2756.C	.2563721+CC1
25	14.5	2848.C	.2649302+CC1
26	15.5	2271.C	.2112558+CC1
27	17.2	4185.C	.2048060+CC1
28	19.1	3319.C	.1668997+CC1
29	21.0	2592.C	.1303331+CC1
30	22.8	1967.C	.9630356+CC1
31	24.7	1343.C	.6752986+CC0
32	26.5	977.C	.4793354+CC0
33	29.4	713.C	.3595167+CC0

COMPUTED EXTINCTION, SCATTERING, AND ABSORPTION COEFFICIENTS (KM\*-1):  
 BETAE= .8940953C+CC1, BETAS= .86801398+CC1, BETAA= .26091324+CC0

TABLE I

The measured density of aerosols at the diameters (μm) shown represent an average of 60 1-second spectra taken over a 4-minute period. The visibility during the period as measured by the MRI Model 1580A visiometer varied between 1.18 and .179 km. Also shown in the table is the forward extinction coefficient (forward scattered plus absorption) computed for a wavelength of .53 μm using the relation

$$k_s = \int_r \pi r^2 N(r) Q_s dr \quad (41)$$

N(r) is the measured distribution of spherical scatterers of radius r, Q<sub>a</sub> and Q<sub>s</sub> are the Mie theory absorption and scattering efficiencies. For the example, the calculated

forward extinction coefficient is  $8.9 \text{ km}^{-1}$ . From the well known relationship ( $V = 3.92/k_{\text{ext}}$ ) relating the visibility and extinction coefficient, a visibility of .438 km is determined using the calculated extinction coefficient. This differs but is in fair agreement with the average value of .68 km measured with the visiometer. This difference probably results from the averaging processes, but the example does establish the credibility of the computer program and measured drop-size distributions.

1 Copyright 1970 by the Institute of Electrical and Electronics Engineers, Inc., Reprinted, with permission, from Proceedings of the IEEE, October 1970, R. M. Lerner and A. E. Holland, "The Optical Scatter Channel," vol. 58, No. 10, pp 1547-1563.

2 It is customary in radiative transfer to make the narrow band assumption, so as to consider the energy  $dE_\nu$  which flows in time  $dt$  from solid angle  $d\Omega$  and within spectral region  $(\nu, \nu + d\nu)$  across area  $dA$  making angle  $\phi$  with the normal to  $dA$ . This defines the specific intensity  $I_\nu$  to be

$$I_\nu = dE_\nu / d\nu dA \cos \phi d\Omega dt.$$

#### 4.0 REFERENCES

1. P. M. Livingston, G. L. Trusty, L. H. Ruhnke and G. C. Mooradian, "Joint NRL/NELC Optical Satellite Communication Atmospheric Propagation Test Plan," Optical SATCOM, Apr 1975.
2. R. J. Giannaris, G. C. Mooradian and W. R. Stone, "CO<sub>2</sub> Coherent Propagation (with Reciprocal Tracking) through the Marine Boundary Layer," NELC Technical Report 1994, 28 Jun 1976.
3. R. M. Lerner and A. E. Holland, "The Optical Scatter Channel," Proceedings of the IEEE, vol. 58, No. 10, pp 1547-1563 (1970).
4. R. A. Dell-Imagine, "A Study of Multiple Scattering of Optical Radiation with Applications to Laser Communication," in Advances in Communication Systems, vol. II, Ed. by V. A. Balakrishnan, Academic Press, New York, pp 1-50 (1966).
5. G. N. Plass, G. W. Kattawar, and F. E. Catchings, "Matrix Operator Theory of Radiative Transfer," App. Opt., vol. 12, No. 2, pp 314-329 (1973).
6. S. Chandrasekhar, Radiative Transfer; Clarendon Press; Oxford, England, reprinted; Dover, New York (1960).
7. V. Kourganoff, Basic Methods in Transfer Problems, Dover, New York (1963).
8. R. Preisendorfer, Radiative Transfer on Discrete Spaces, Pergamon Press, New York (1965).
9. H. C. van DeHulst, Light Scattering by Small Particles, Wiley New York (1957).

10. M. Born and E. Wolf, Principle of Optics, Pergamon Press, New York (1970).
11. M. Kerker and Milton, The Scattering of Light and other Electromagnetic Radiation, Academic Press, New York (1969).
12. E. A. Bucher, "Computer Simulation of Light Pulse Propagation for Communication through Thick Clouds," App. Opt., vol. 12, No. 10, pp 2391-2400 (1973).
13. J. V. Dare and J. Gazdag, "A Modified Fourier Transform Method for Multiple Scattering Calculations in a Plane Parallel Mie Atmosphere," App. Opt., vol. 9, No. 6, pp 1457-1466 (1970).
14. A. Papoulis, Probability, Random Variables, and Stochastic Processes, McGraw-Hill, New York (1965).
15. A. Papoulis, Systems and Transforms with Applications in Optics, McGraw-Hill, New York (1968).
16. A. Ishimaru, "Correlation Functions of Wave in a Random Distribution of Stationary and Moving Scatterers," Radio Science, vol. 10, No. 1, pp 45-52 (1975).
17. P. Livingston, private communication.
18. R. Lutomirski, private communication.
19. R. L. Fante, "Mutual Coherence Function and Frequency Spectrum of a Laser Beam Propagating through Atmospheric Turbulence," J.O.S.A., vol. 64, No. 5, pp 592-598 (1974).
20. G. N. Plass and G. W. Kattawar, "Monte Carlo Calculations of Light Scattering from Clouds," App. Opt., vol. 7, No. 3, pp 415-419 (1962).
21. H. M. Heggestad, "Optical Communication through Multiple Scattering Media," M.I.T. Technical Report No. 472, 22 November 1968.
22. H. C. van de Hulst, Bull. Astron. Inst., Neth., vol. 20, p 77 (1968).
23. R. E. Danielson, D. R. Moore, and H. C. van de Hulst, J. Atmos. Sci., vol. 26, p 1078 (1968).
24. E. A. Bucher and R. M. Lerner, "Experiments on Light Pulse Communication through Atmospheric Clouds," App. Opt., vol. 12, p 2401 (1973).
25. E. A. Bucher, "Propagation Models for Optical Communication through Fog and Clouds," Proceedings of the National Electronics Conference, vol. 29, p 180 (1974).